Geochemistry, Geophysics, Geosystems®

AGU ADVANCING EARTH AND SPACE SCIENCES

RESEARCH ARTICLE
10.1029/2025GC012720

Constraints on Noble Gas Variability in OIB and MORB From Non-Equilibrium Magmatic Degassing Models

Thomas Williams[1], **Stephen Parman**[1], **and Christian Huber**[1]

[1]Department of Earth, Environmental, and Planetary Sciences, Brown University, Providence, RI, USA

Key Points:

- We model ^{3}He and ^{22}Ne fractionation during open- and closed-system degassing
- Degassing pathways do not reproduce the observed range of ^{3}He and ^{22}Ne in OIB and MORB
- Disequilibrium degassing cannot resolve the "Helium Paradox"

Supporting Information:

Supporting Information may be found in the online version of this article.

Correspondence to:

T. Williams,
thomas_williams@brown.edu

Citation:

Williams, T., Parman, S., & Huber, C. (2026). Constraints on noble gas variability in OIB and MORB from non-equilibrium magmatic degassing models. *Geochemistry, Geophysics, Geosystems*, *27*, e2025GC012720. https://doi.org/10.1029/2025GC012720

Received 2 OCT 2025
Accepted 5 MAR 2026

Author Contributions:

Conceptualization: Thomas Williams, Stephen Parman
Data curation: Thomas Williams
Formal analysis: Thomas Williams, Christian Huber
Investigation: Thomas Williams, Stephen Parman, Christian Huber
Methodology: Thomas Williams, Christian Huber
Project administration: Stephen Parman
Resources: Thomas Williams, Christian Huber
Software: Thomas Williams, Christian Huber
Supervision: Stephen Parman, Christian Huber
Validation: Thomas Williams

Abstract Noble gas concentrations in ocean island basalts (OIB) and mid-ocean ridge basalts (MORB) are affected by degassing processes, obscuring their pre-eruptive characteristics. Degassing corrections commonly assume near-equilibrium partitioning of noble gases between melt and vapor. However, kinetic disequilibrium has been proposed as a mechanism capable of modifying noble gas ratios. For example, kinetic effects may allow OIBs to exhibit lower ^{3}He contents than MORBs, even if OIB plumes sample a low $^{4}He/^{3}He$ "undegassed" primordial lower mantle—the so-called "Helium Paradox" (Gonnermann & Mukhopadhyay, 2007, https://doi.org/10.1038/nature06240). It has also been suggested that kinetic effects allow OIB and MORB to share a homogeneous pre-degassing $^{3}He/^{22}Ne$ ratio. Despite this, inferred mantle compositions may not require the presence of an "undegassed" reservoir, and there is evidence that OIB and MORB sources exhibit heterogenous $^{3}He/^{22}Ne$ ratios. Here, we model the kinetics of CO_2 and noble gas exchange between bubbles and melt within a three-stage framework for magmatic ascent to evaluate the magnitude of non-equilibrium fractionation. The first and third stages treat the kinetics of bubble growth during closed-system decompression, whilst the second treats gas exchange between ascending bubbles and a melt at rest within a shallow, open-system, sub-volcanic reservoir. Across plausible ranges of ascent rate, bubble populations, and noble gas diffusivity, our results indicate that disequilibrium cannot produce variations in ^{3}He contents and $^{3}He/^{22}Ne$ ratios sufficient to reproduce the range observed in OIB and MORB. Therefore, OIB and MORB sources cannot share a homogenous $^{3}He/^{22}Ne$ ratio, and disequilibrium does not resolve the "Helium Paradox."

Plain Language Summary Noble gases such as helium and neon trapped in mid-ocean ridge basalts and ocean-island basalts are key tracers for understanding the structure and evolution of the Earth's mantle. However, as magmas rise and release gases, this degassing strips noble gases from the melt, modifying their concentrations. Although many studies assume that noble gases remain in equilibrium with the melt during degassing, it has been suggested that magmatic ascent or melt-vapor separation may be too rapid for diffusion to allow noble gases to reach equilibrium concentrations. These effects could explain why ocean-island basalts often contain less ^{3}He than mid-ocean ridge basalts, even though ocean-island basalts may sample a less-degassed mantle (a phenomenon known as the "Helium Paradox"). To determine the magnitude of disequilibrium effects, we modeled gas exchange between bubbles and melt during magmatic ascent in a closed-system (where bubbles and melt remain coupled to one another) and an open-system (where bubbles escape the melt). Our results show that disequilibrium cannot account for observed ^{3}He and $^{3}He/^{22}Ne$ differences between ocean island and mid-ocean ridge basalts. Instead, these differences reflect mantle source variations, and disequilibrium degassing does not resolve the "Helium Paradox."

1. Introduction

Noble gas concentrations and ratios recorded in mid-ocean ridge basalt (MORB) and ocean island basalt (OIB) glasses are modified from their mantle source values through partitioning into the vapor phase during magmatic degassing (Aubry et al., 2013; Iacono-Marziano et al., 2010; Moreira & Kurz, 2012). To enable noble gas concentrations and isotope ratios to provide insights into Earth's accretion, differentiation, and long-term evolution, it is common to correct for this degassing by assuming equilibrium, solubility-based partitioning between vapor and melt (Allègre et al., 1983; Parai, 2024; Stracke et al., 2022; Tucker et al., 2018). However, correcting for equilibrium degassing does not resolve the so-called "Helium Paradox." This "Paradox" arises when the low $^{4}He/^{3}He$ ratios observed in OIBs are interpreted as evidence for sampling of a "primordial," less-degassed mantle reservoir by mantle plumes (Anderson, 1998; Hilton & Porcelli, 2014). If OIBs sample this high ^{3}He mantle reservoir, they should have much higher pre-degassing ^{3}He concentrations than MORBs. Instead, OIBs cluster

Visualization: Thomas Williams
Writing – original draft: Thomas Williams
Writing – review & editing: Thomas Williams, Stephen Parman, Christian Huber

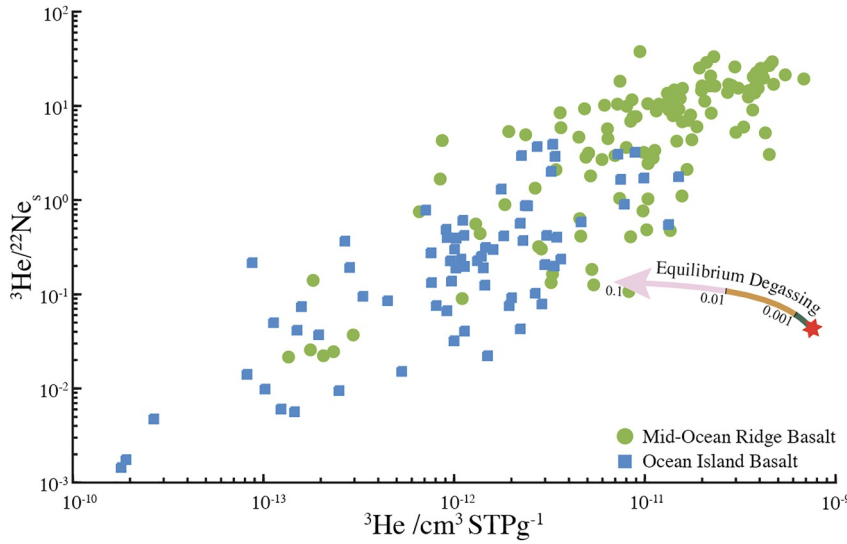

Figure 1. Global compilation of noble gas contents in basalts. Green circles and blue squares correspond to MORB and OIB step heating analyses of submarine glasses respectively. The arrow represents an illustrative equilibrium closed-system degassing trajectory originating from an arbitrary initial composition, colored by discrete vesicularity bins ($\phi < 0.001$, $0.001 \leq \phi \leq 0.01$, $0.01 < \phi \leq 0.1$). The proportion of CO_2 lost from the melt is a function of pressure; at 1 kbar, these vesicularity ranges correspond to losses of <17%, 17 to ~64%, and ~64 to 95% of CO_2, respectively. For details on degassing calculations, please see the text. This demonstrates that equilibrium degassing does not control the basaltic ^{3}He -$^{3}He/^{22}Ne$ array. Noble gas data is compiled from references in Yamamoto and Kurz (2022), and is segmented by sample location in Figures S1 and S2 of Supporting Information S1. We filter these samples by their $^{20}Ne/^{22}Ne$ ratio to assess the impact of atmospheric contamination in Figure S3 of Supporting Information S1.

toward lower ^{3}He concentrations than MORBs (Figure 1). If OIBs start with higher ^{3}He concentrations, this implies that they are more extensively degassed than MORBs.

Under equilibrium degassing conditions, the maximum fractionation between He and Ne for a single stage of vesiculation will be the ratio of their solubilities:

$$\frac{C_{He}/C_{Ne}}{C^{0}_{He}/C^{0}_{Ne}} = \frac{S_{He}}{S_{Ne}} \quad (1)$$

where C represents the final concentration, C^{0} the initial concentration, and S the solubility of each species in the melt (Jambon et al., 1986). Ne is less soluble than He; thus, during progressive degassing, Ne is preferentially exsolved, causing the $^{3}He/^{22}Ne$ ratio of the residual melt to increase relative to its initial value (Aubry et al., 2013; Iacono-Marziano et al., 2012a; E. B. Watson, 2017). In a global compilation of MORB and OIB glasses, low ^{3}He concentrations are associated with low $^{3}He/^{22}Ne$ ratios, a relationship that is, inconsistent with the monotonic increase in $^{3}He/^{22}Ne$ produced by equilibrium, solubility-controlled degassing (annotated arrow in Figure 1). Therefore, solubility-controlled degassing cannot be the primary control on $^{3}He/^{22}Ne$ ratio in basaltic glasses (Anderson, 1998; Burnard, 1999; Gonnermann & Mukhopadhyay, 2007).

The apparent contradiction between high ^{3}He contents in pre-degassed OIB sources, and low ^{3}He contents combined with low $^{3}He/^{22}Ne$ ratios in degassed OIB samples, may be reconciled by accounting for kinetic effects during degassing (Gonnermann & Mukhopadhyay, 2007). If the timescales of magmatic ascent or melt-vapor separation are short relative to He or Ne diffusion timescales, noble gas exsolution becomes kinetically limited. Because Ne diffuses more slowly than He, disequilibrium effects inhibit Ne loss to the vapor phase to a greater extent than they inhibit He loss, potentially reducing or reversing the increase in $^{3}He/^{22}Ne$ ratios associated with equilibrium degassing (Gonnermann & Mukhopadhyay, 2007). Disequilibrium degassing may therefore allow for OIBs to have higher initial ^{3}He concentrations and $^{3}He/^{22}Ne$ ratios than MORBs, consistent with the presence of a "primordial" mantle reservoir. This implication could reinforce the discrepancies between geochemical models that argue for an isolated lower mantle, and geophysical observations suggesting that the

mantle is well mixed (Albarède, 2008; Deng et al., 2023; Gülcher et al., 2021; Parai, 2024; Stracke et al., 2022). It would also allow OIB and MORB sources to share similar pre-degassing $^{3}He/^{22}Ne$ ratios, supporting "Steady State" mantle models in which fluxes of noble gases into and out of the upper mantle are balanced, and the lower mantle has remained a closed system over ~4.5 Ga (Gonnermann & Mukhopadhyay, 2007; Porcelli & Wasserburg, 1995a, 1995b; Weston et al., 2015). Conversely, if disequilibrium degassing cannot account for these observations, alternative mechanisms are required, such as models that account for low $^{4}He/^{3}He$ in OIBs without invoking an isolated mantle component (e.g., Bouhifd et al., 2020; Dygert et al., 2018; Gonnermann & Mukhopadhyay, 2009; Horton et al., 2023; M. G. Jackson et al., 2021; Olson & Sharp, 2022; Parman, 2007; Wang et al., 2022), and models that suggest that $^{3}He/^{22}Ne$ differences between OIBs and MORBs reflect mantle source heterogeneity (e.g., Honda et al., 1993; Parai, 2024; Tucker & Mukhopadhyay, 2014; Yamamoto & Kurz, 2022).

Non-equilibrium noble gas fractionation have been inferred to affect both MORB and OIB samples (Aubaud et al., 2004; Paonita & Martelli, 2006; Tucker et al., 2018). More significantly, Gonnermann and Mukhopadhyay (2007) and Weston et al. (2015) propose that disequilibrium degassing can resolve the "Helium Paradox" through disequilibrium degassing while permitting MORB and OIB sources to share homogeneous $^{3}He/^{22}Ne$ ratios. Their models have allowed for better insights into noble gas behavior during degassing. However, the two frameworks yield contrasting results, reflecting differences in their physical treatment of degassing, most notably in how major-volatile loss is partitioned across degassing steps. Additionally, noble gas diffusion coefficients in basaltic melts remain poorly constrained (Figure S4 in Supporting Information S1), and the wide range of values adopted across studies contribute to conflicting model outcomes. As a result, some models support disequilibrium degassing as a solution to the "Helium Paradox" (Gonnermann & Mukhopadhyay, 2007; Weston et al., 2015), whereas others conclude that disequilibrium alone is insufficient (Tucker et al., 2018). In light of isotope-element ratio analyses indicating that kinetic fractionation from a single reservoir cannot explain the full range of MORB and plume systematics (Parai et al., 2019), it is apparent that there is a need for better constraints on diffusion parameters and degassing dynamics to evaluate the viability of noble gas disequilibrium models.

Here, we aim to more closely constrain the contribution of kinetic effects to measured noble gas ratios and abundances in MORB and OIB glasses. We first define degassing stages based on the relative magnitudes of melt ascent velocity, bubble-melt separation velocity, and the time available for vapor-melt separation. The three resulting stages are: (1) initial bubble growth and ascent; (2) storage in a magma reservoir; and (3), ascent to seafloor (Figure 2). Immediately after bubble nucleation (Stage 1), the low Stokes velocities of small bubbles mean that bubbles remain coupled to the melt over the timescales of melt ascent, and the system can be considered closed. In contrast, for bubbles within a stalled magma in a shallow magma reservoir (Stage 2), there is sufficient time for bubbles to decouple from melt, resulting in open-system degassing (Parmigiani et al., 2016; Wanless & Shaw, 2012). Finally, during ascent of magma to the seafloor (Stage 3), bubble-melt separation velocities are greater than in Stage 1 due to the combined effects of mechanical expansion and reduced CO_2 solubility on bubble growth. However, for inferred timescales of magmatic ascent, bubble-melt separation distances are still limited, and the system can again be considered closed (Bamber et al., 2024). We model both closed-system (no loss or gain of volatiles in a given magma parcel), and open system (differential movement of vapor bubbles and melt) degassing by treating He and Ne as passive tracers in a similar manner to Gonnermann and Mukhopadhyay (2007), Weston et al. (2015), E. B. Watson (2017), and Tucker et al. (2018). To investigate closed-system degassing, we build a 2D model in which we explicitly account for pressure- and diffusion-driven bubble growth, melt viscosity, and bubble geometry. We explore how magmatic CO_2 content, decompression rate, the pressure range during degassing, and bubble size influences ^{3}He concentrations and $^{3}He/^{22}Ne$ ratios. Next, we derive a model for open-system degassing, incorporating both bubble advection and the effects of CO_2 supersaturation during the ascent of melt into a magma reservoir, and assess the roles of magmatic volatile contents, melt-bubble separation velocity, and partitioning during bubble growth on controlling noble gas loss. For both open- and closed-system degassing, we determine the extent to which kinetic effects enable resolution of the "Helium Paradox."

2. Methods

2.1. Closed-System Degassing (Stages 1 and 3)

2.1.1. Physical Model

As pressure decreases during magmatic ascent, CO_2 and H_2O become progressively less soluble in the melt, and the resultant supersaturation results in bubble nucleation (Dixon, 1997); noble gases then partition between

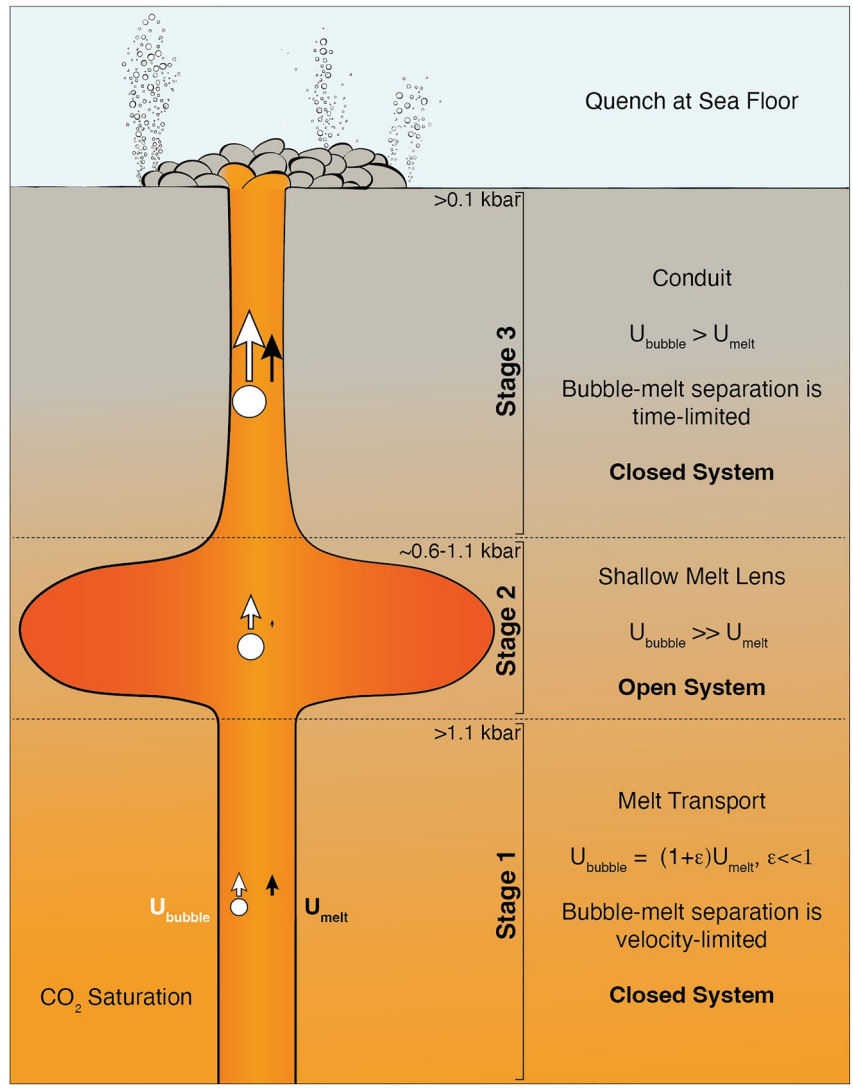

Figure 2. Schematic illustration of the magmatic system, showing the three mass transport stages considered in our modeling approach. In Stage 1, following bubble nucleation, low bubble–melt separation velocities (Stokes velocities) inhibit decoupling, and the system is treated as closed. In Stage 2, we consider stalled magma within a shallow melt lens (Wanless & Shaw, 2012), where a prolonged residence time allows for bubble–melt separation even at low ascent velocities, as the melt ascent velocity (U_{melt}) is small relative to the bubble ascent velocity (U_{bubble}) (Parmigiani et al., 2016). In Stage 3, bubble ascent velocities are high due to growth via diffusion and mechanical expansion, but rapid melt ascent limits the time available for melt–bubble separation (Bamber et al., 2024). Illustrative pressures associated with melt lenses are taken from M. Jones et al. (2018) and Arnulf et al. (2014); these correspond to a melt lens depth of ~1.1–2.3 km below the seafloor. This diagram is conceptual; our modeling approach does not assume a specific system geometry.

bubbles and the melt (Aubry et al., 2013). We consider that bubbles and melt remain coupled to one another during ascent when bubble-melt separation distances are low relative to the half-distance L between bubbles. In other words, the system is closed when the condition $U_b \cdot t_{dec} < L$ is satisfied, where U_b is the bubble-melt separation velocity, and t_{dec} is the decompression timescale. This applies during stages 1 and 3 of our conceptual model (Figure 2). We therefore model the diffusion and exsolution of noble gases from the melt into a bubble during ascent to a magma reservoir (Stage 1) or to the seafloor (Stage 3) as operating within a closed system. Because CO_2 saturates at substantially higher pressures than H_2O in basaltic melts we treat the vapor phase as pure CO_2, and neglect H_2O in the bubble (Dixon, 1997; Iacono-Marziano et al., 2012b). During ascent, the bubble grows via two mechanisms: (a) mechanical expansion of the gas due to decreasing pressure; and (b), diffusion-driven degassing from the CO_2-supersaturated melt into the bubble. Bubble growth is resisted by the viscosity of

the melt (Lensky et al., 2004). Growth decreases the partial pressure of the noble gases in the bubble, providing a driving force for further diffusion of noble gases into the bubble. For magmatic ascent from depth to a magma reservoir (Stage 1), we consider closed-system degassing to end once the magma parcel reaches the pressure of the magma reservoir. When magma rises to the seafloor (Stage 3), the melt is assumed to quench instantaneously under the hydrostatic pressure of the overlying water column, halting both bubble growth and diffusive exchange. In both stages, all volatile loss from the melt is assumed to occur via gas transfer into pre-existing bubbles, with no secondary nucleation events. The noble gases are treated as passive tracers, contributing negligibly to the bubble's partial pressure (E. B. Watson, 2017).

2.1.2. Numerical Method

We model our system by adapting the lattice Boltzmann method (LBM) bubble-growth model of Huber et al. (2014) to capture the behavior of the noble gases by treating them as chemically diffusing tracers. This model is in turn a modification of the free surface model proposed by Körner et al. (2005). Here, we briefly introduce the model, and describe the modifications we made to model noble gas diffusion. For more details, the reader is referred to Huber et al. (2014) and Körner et al. (2005).

Within the LBM, the Boltzmann equation

$$\frac{\partial f}{\partial t} + \boldsymbol{\xi} \cdot \nabla f = \Omega_f \tag{2}$$

is discretized in both physical and velocity space. Here, the probability distribution function $f(\mathbf{x}, \boldsymbol{\xi}, t)$, is defined such that $f(\mathbf{x}, \boldsymbol{\xi}, t) d\mathbf{x} d\boldsymbol{\xi}$ represents the number of particles in the phase space element $d\mathbf{x} d\boldsymbol{\xi}$ at a given time t, $\mathbf{x}$ denotes the spatial coordinates on the lattice, and Ω_f is the collision operator. In the LBM, particle distribution functions (PDFs) are defined at each lattice site, stream along a finite set of discrete velocity vectors ($\mathbf{e_i}$) and reach a neighboring site at the next time step. We use a two-dimensional, five-velocity (D2Q5) lattice for chemical (CO_2, He, Ne) diffusion, and a D2Q9 lattice for the fluid dynamics component, with velocity vectors defined as:

$$\mathbf{e_i} = \begin{cases} (0,0) & \text{if } i = 0 \\ \left(\cos\left(\frac{(i-1)\pi}{2}\right), \sin\left(\frac{(i-1)\pi}{2}\right)\right) & \text{if } i = 1, \ldots, 4 \\ \left(\cos\left(\frac{(2i-1)\pi}{4}\right), \sin\left(\frac{(2i-1)\pi}{4}\right)\right) & \text{if } i = 5, \ldots, 8 \end{cases} \tag{3}$$

The evolution of the PDFs is governed by a linearized collision operator, and here we adopt a lattice version of the Bhatnagar–Gross–Krook model (Bhatnagar et al., 1954; Qian, 1993). The update of the PDF f_i between consecutive time steps t and $t + 1$ involves two sequential steps: a collision step

$$f_i^{\text{out}}(\mathbf{x}, t) = f_i(\mathbf{x}, t) + \frac{1}{\tau_F}\left[f_i^{\text{eq}}(\mathbf{x}, t) - f_i(\mathbf{x}, t)\right] + F_i \tag{4a}$$

followed by a streaming step

$$f_i^{\text{in}}(\mathbf{x} + \mathbf{e}_i, t + 1) = f_i^{\text{out}}(\mathbf{x}, t). \tag{4b}$$

F_i is a body force term, τ is the relaxation time—explicitly related to the kinematic viscosity ν of the fluid (τ_f) or the diffusion coefficient D of the volatile species (τ_j) through the equations

$$\nu = c_s^2\left(\tau_f - \frac{1}{2}\right) \qquad D_j = c_s^2\left(\tau_j - \frac{1}{2}\right) \tag{5}$$

—and f_i^{eq} is the local equilibrium distribution function:

$$f_i^{\mathrm{eq}}(\mathbf{x},t) = w_i\rho(\mathbf{x},t)\left[1 + \frac{\mathbf{u}\cdot\mathbf{e}_i}{c_s^2} + \frac{1}{2}\left(\frac{\mathbf{u}\cdot\mathbf{e}_i}{c_s^2}\right)^2 - \frac{1}{2}\frac{\mathbf{u}\cdot\mathbf{u}}{c_s^2}\right]. \tag{6}$$

In this equation, ρ is the fluid density, $\mathbf{u}$ is the macroscopic velocity, c_s^2 is the lattice speed of sound, and w_i are the lattice weights. It was shown via Chapman-Enskog expansion that the solution to Equations 4a–6 retrieves the Navier Stokes equations together with coupled advection-diffusion equations for the concentration of CO_2 and noble gases (Huber et al., 2014).

For the coupling between bubbles and melt, we use the free surface model developed by Körner et al. (2005), which uses an approach similar to the Volume-of-Fluid method. The lattice is divided among three cell types: gas, melt, and interface. Bubble movement and expansion changes the volume fraction of melt ϵ at each site, resulting in the evolution of cell types. The cell type is therefore updated dynamically according to the fluid mass content of the cell m. The continuous scalar quantity m is updated by tracking mass exchange between neighboring lattice sites:

$$\Delta m_i(\mathbf{x},t) = \begin{cases} 0 & \text{if } \mathbf{x} \in \text{gas cell} \\ \Delta f_i^{\mathrm{out}} \equiv f_i^{\mathrm{out}}(\mathbf{x}+\mathbf{e}_i,t) - f_i^{\mathrm{out}}(\mathbf{x},t) & \text{if } \mathbf{x} \in \text{melt cell} \\ \frac{1}{2}(\epsilon(\mathbf{x},t) + \epsilon(\mathbf{x}+\mathbf{e}_i,t))\Delta f_i^{\mathrm{out}} & \text{if } \mathbf{x} \in \text{interface cell} \end{cases} \tag{7a}$$

$$m(\mathbf{x},t+1) = m(\mathbf{x},t) + \sum_{i=0}^{8} \Delta m_i(\mathbf{x},t). \tag{7b}$$

In the free surface algorithm, the effect of the bubble at the interface with the melt is an imposed pressure boundary condition, detailed in Körner et al. (2005). We assume that the bubbles are inviscid and treat the bubble-melt boundary condition as a free surface that does not support tangential stress, but does permits a normal stress discontinuity due to surface tension and the density contrast between two fluids (Huber et al., 2014). The CO_2 bubble behaves as an ideal gas, and the interfacial pressure is modified by surface tension (σ) and the disjoining pressure (Π) due to the interaction of two melt-gas interfaces, giving the following equation for pressure:

$$P_g(\mathbf{x},t) = \frac{n(t)RT}{V(t)} - 2\kappa(\mathbf{x},t)\sigma - \Pi, \tag{8}$$

where n is the number of moles of gas molecules in a given bubble, V the volume, T the ambient temperature, R the ideal gas constant, and $\kappa(\mathbf{x},t)$ the local curvature of the interface.

During our imposed decompression, the bubbles will grow due to the combined effects of mechanical expansion and diffusive exchange through a reduction in CO_2 solubility in the melt. We assume a pressure reference frame where the pressure in the ambient melt is constant over a given run, but the mechanical pressure ($P_{\mathrm{g,mech}}$) inside bubbles evolves due to the imposed decompression rate $(dP/dt)_{\mathrm{dec}}$ (Huber et al., 2014). If bubble growth is impeded by surface tension and viscous stresses in the melt, the mechanical pressure inside the bubble will increase. In this reference frame, the mechanical pressure evolution in bubbles is given by:

$$\frac{dP_{\mathrm{g,mech}}}{dt} = RT\left[\frac{1}{V}\frac{dn}{dt} - \frac{n}{V^2}\frac{dV}{dt}\right] - \left(\frac{dP}{dt}\right)_{\mathrm{dec}}. \tag{9}$$

To allow for bubble expansion, we impose a free surface with a fictitious "atmosphere" at the top of the system, which is a special case of a bubble cell with a no-flux condition for CO_2 and the noble gases.

We account for diffusion of dissolved volatiles in the melt to track the loss of He and Ne from the melt, and to grow the bubble through CO_2 diffusion (Equation 9). We use a similar approach to Körner et al. (2005), where two additional PDFs for CO_2 (g_i) and the noble gases (h_i) are used to model an advection-diffusion equation with an imposed concentration boundary condition at the bubble-melt interfaces.

The boundary condition for the dissolved volatile concentration at a bubble-melt interface is imposed to follow Henry's law.

$$C_b(\mathbf{x},t) = K_H(P_g \cdot \chi)^{\epsilon_H}, \quad \mathbf{x} \in \text{Interface cell} \tag{10}$$

where the total pressure in the bubble is obtained from Equation 8, and the mole fraction χ of the noble gas i in the bubble is given by:

$$\chi_i = \frac{n_i}{\sum_{j=1}^{N} n_j}. \tag{11}$$

In this way, we implicitly link the behavior of the noble gases to a decompression path, leading to time-dependent partitioning behavior. The boundary condition at the interface site is then imposed by setting the missing distributions g_x (coming from the adjacent gas cell) to:

$$g_x = \begin{cases} g_x^{\text{eq}}(C_b,\mathbf{u}) + g_{\bar{x}}^{\text{eq}}(C_b,\mathbf{u}) - g_{\bar{x}}(C_b,\mathbf{u}) & \text{if } \mathbf{x} \in \text{bubble cell} \\ g_x^{\text{eq}}(C_b,\mathbf{u}) - g_{\bar{x}}^{\text{eq}}(C_b,\mathbf{u}) + g_{\bar{x}}(C_b,\mathbf{u}) & \text{if } \mathbf{x} \in \text{atmosphere cell} \end{cases} \tag{12}$$

while the other distributions are set to $g_j(C_b,\mathbf{u})$. The same boundary condition applies to $h_j(C_b,\mathbf{u})$. A detailed description of benchmark problems solved with the generic free surface lattice Boltzmann model can be found in Körner et al. (2005). We validate single-bubble growth within our LBM model against the analytical solution for equilibrium bubble growth within a radially symmetric melt shell of Lensky et al. (2004), which we solve in 2D for an infinite cylinder geometry (Figures S5 and S6 in Supporting Information S1). This solution is valid when the gas pressure follows the ambient pressure, and the concentration in the melt shell is uniform according to the solubility at the ambient pressure.

2.1.3. Physical Parameters

We determine Henry's law parameters for of $K_H^{CO_2} = 1.5 \times 10^{-9}$ mol g^{-1} bar^{-1} and $\epsilon_H^{CO_2} = 1.276$ by fitting a power law to the solubility of a pure CO_2 volatile phase in a basaltic melt (Figure S7 in Supporting Information S1) using the VesiCAL implementation of MagmaSat (Iacono-Marziano et al., 2012a; Iacovino et al., 2021). For the noble gases, we use values of $K_H^{He} = 2.7 \times 10^{-8}$ and $K_H^{Ne} = 8.0 \times 10^{-9}$ mol g^{-1} bar^{-1} and $\epsilon_i = 1$ following Gonnermann and Mukhopadhyay (2007). We note that these coefficients are not significantly different to those determined using the semi-empirical model of Iacono-Marziano et al. (2010), but that the exact ratio of He to Ne solubility is a function of pressure, temperature and chemical composition. For the melts considered here, this results in a ratio K_H^{He}/K_H^{Ne} change of ~2 over a space of 0.5–5 kbar and 1373K–1573K (Iacono-Marziano et al., 2010). We do not consider the effects of melt CO_2 and H_2O, which may significantly reduce the solubility difference between He and Ne (Nuccio & Paonita, 2000; Paonita, 2009). Melt viscosity is calculated using the parametrization of Giordano et al. (2008). At the start of each simulation, bubble seeds with an initial radius of $10^{-5} \leq R_b \leq 10^{-4}$ m are set in a periodic array, and we initialize with a bubble volume fraction ϕ of 0.005–0.1, consistent with measured CO_2 contents in basalts and bubble fraction observations (Chavrit, 2010; Voyer et al., 2019). No secondary nucleation event is considered.

For CO_2 diffusion coefficient values, we use the parametrization of Ni and Keppler (2013). For the noble gas diffusion coefficients, we follow Tucker et al. (2018) and use values of $D_{He} = 10^{-8.5}$, $D_{Ne} = 10^{-9.0}$, and $D_{Ar} = 10^{-10.5}$ m^2 s^{-1}. We caution, however, that currently available diffusion coefficients for He, Ne, and Ar are subject to considerable uncertainty, as demonstrated in Figure S4 of Supporting Information S1. Values for the full suite of noble gas diffusivities in a basaltic melt have only been obtained experimentally once, but the results were preliminary and have not been reproduced (Lux, 1987). Additionally, these values are over one order of magnitude slower than Ar and He diffusivities derived from synthetic iron-free basalts and CMAS melts (Amalberti et al., 2018; Nowak et al., 2004). Furthermore, they disagree with diffusivities derived from molecular dynamics simulations (Guillot & Sator, 2012). This may be due to compositional differences, but the influence of melt composition on noble gas diffusion is unconstrained (Behrens, 2010). Despite this uncertainty, studies have

not found a difference between D_{He} and D_{Ne} exceeding approximately one order of magnitude in basaltic melts, or in glasses at temperatures above 1250K, when evaluated for a single composition (Behrens, 2010; Guillot & Sator, 2012; Lux, 1987).

We adopt the same initial MORB ^{3}He concentration as Gonnermann and Mukhopadhyay (2007) (10^{-8} cm^{3}STP/g) to facilitate direct comparison with their results. The initial ^{3}He/^{22}Ne ratio is set to 3.375, corresponding to the partitioning ratio of He and Ne in basaltic melts. This value is slightly lower than that assumed by Gonnermann and Mukhopadhyay (2007), but remains within the range inferred for MORB and OIB mantle sources (Yamamoto & Kurz, 2022).

2.2. Open-System Degassing (Stage 2)

2.2.1. Physical Model

In a stagnant melt, the residence time t_{res} is such that there is sufficient time for bubbles to separate from melt even if bubble-melt separation velocities are low. In other words, if $U_b \cdot t_{res} \gg L$, open system degassing takes place (Stage 2 in Figure 2). We assume that this condition applies within a shallow melt reservoir beneath a mid-ocean ridge (e.g., Arnulf et al., 2014; Carbotte et al., 2021), and we ignore the effects of turbulence and convection within the reservoir. We evaluate the governing noble gas transport processes in this system by casting the simplified 1D coupled mass conservation equations of Huber et al. (2012) into non-dimensional form (detailed fully in Text S2 of Supporting Information S1). We do so by first introducing the characteristic length scale L, concentration scale C_0, and time scale of bubble ascent $t^* = tU_b/L$. Here, the velocity scale

$$U_b = \frac{(\rho_m - \rho_g)\, g R_b^2}{3\mu_m} \tag{13}$$

is given by the steady state separation (ascent) velocity of a single bubble via the Hadamard-Rybczynski solution where internal viscosity is insignificant (Hadamard, 1911; L. E. Jackson et al., 2022; Rybczynsk, 1911). Gravitational acceleration is given by g, bubble radius by R_b, and the melt's dynamic viscosity by μ_m. The effect of hydrodynamic interactions between bubbles on U_b is implemented using the hindrance function of Faroughi and Huber (2015).

This scaling results in the non-dimensional coupled 1-D transport equations:

$$\frac{\partial C_i^{g*}}{\partial t^*} + \frac{\partial C_i^{g*}}{\partial z^*} - \frac{M}{\mathrm{Pe}_i}\left(C_i^{m*} - K_i C_i^{g*}\right) = 0 \tag{14a}$$

$$\frac{\partial C_i^{m*}}{\partial t^*} + \frac{1}{\mathrm{Pe}_i}\left(C_i^{m*} - K_i C_i^{g*}\right) = 0 \tag{14b}$$

M represents the non-dimensional mass ratio of melt to gas—$M = (1 - \phi)\rho_m/(\phi\rho_g)$—where ϕ is the vapor fraction in the melt, ρ_m the melt density, and ρ_g the vapor density. The ratio of advective to diffusive flux is condensed into the dimensionless Péclet number:

$$\mathrm{Pe}_i = \frac{U_b L}{D_i} \tag{15}$$

where D_i is the diffusion coefficient of element i. The superscripts m and g represent the melt and gas/vapor phase respectively, and K_i is the gas-melt partition coefficient of element i.

2.2.2. Numerical Method

The coupled mass conservation equations for each fluid phase are solved numerically using an implicit finite difference method. The initial concentrations C_i^g and C_i^m for each noble gas are determined analytically for equilibrium conditions ($t = \infty$). The effective partition coefficient K_i is then defined as:

$$K_i = \frac{C_i^{g,\infty}(P, C_{CO_2})}{C_i^{m,\infty}(P, C_{CO_2})}. \quad (16)$$

This procedure is detailed fully in Text S2 of Supporting Information S1.

We take the distance H ascended by the bubble to be the same as the half distance between bubbles, effectively forming a representative periodic unit cell. Over this distance, we treat the pressure as uniform and neglect the hydrostatic drop. As such, the associated change in solubility and gas density over H is negligible. Consequently, if the bubble is in equilibrium with the melt before the initiation of open-system degassing, then the boundary condition and initial conditions are defined by equilibrium melt-vapor partitioning, and subsequent disequilibrium fractionation does not occur. In the other extreme, if a bubble is assumed to nucleate and grow instantly such that it is devoid of noble gases, then the initial and boundary condition for the gas phase in Equation 14 will be defined by $C_i^{g*} = 0$. However, bubbles do not nucleate and grow instantly, and the growth history of the bubbles must be considered when defining the initial conditions.

To address this, we assume that bubbles nucleate at depth during ascent toward the melt reservoir once the melt becomes supersaturated with respect to CO_2, and they remain coupled to the melt during ascent. We then apply our LBM model for closed-system degassing to determine the distributions of noble gases and CO_2 between bubble and melt upon entry into the magma reservoir; these outputs define the initial and boundary conditions for open-system degassing. Because He and Ne diffuse significantly faster in the melt than CO_2, they are in near-equilibrium with the melt upon entry into the reservoir (Section 3.1). In contrast, if ascent is sufficiently rapid that diffusion cannot maintain equilibrium between dissolved carbon in the melt and CO_2 vapor within vesicles, dissolved CO_2 contents may exceed equilibrium solubility at the reservoir pressure. Magma ascent rates from the lower crust vary widely across global ridge systems, ranging from ~0.002 to 0.1 m s^{-1} (Ma et al., 2024; Mutch et al., 2019). Toward the upper end of this range, CO_2 supersaturation develops during decompression (Chavrit et al., 2012).

To bound the maximum noble gas loss during open-system degassing, we impose that upon entry of magma into the reservoir, CO_2 instantaneously attains its equilibrium distribution between bubble and melt. If the melt is supersaturated following ascent, this equilibration results in bubble growth. We neglect noble gas diffusion during this instantaneous equilibration step. Therefore, bubble growth dilutes vapor-phase noble gases, reduces their partial pressures, and generates chemical potential gradients that drive subsequent noble gas diffusion. This extreme bubble-growth end-member is used solely to place an upper bound on kinetic fractionation, not to represent reservoir dynamics or bubble growth processes in detail; as such, this approach will exaggerate the degree of disequilibrium that may develop during open-system degassing.

2.2.3. Physical Parameters

For the density of CO_2 we utilize the Lee–Kesler equation of state for pure CO_2 (Duan & Zhang, 2006). We calculate melt density using the DensityX python library (Iacovino & Till, 2019). All other relevant parameters, including the initial ^{3}He concentration and ^{3}He/^{22}Ne ratio, are fixed to the values adopted for the closed-system degassing model, ensuring that differences between models reflect degassing behavior rather than differing initial conditions.

3. Results

3.1. The Effects of Closed-System Degassing

We consider degassing to occur under closed-system conditions during magmatic ascent to a magma reservoir and to the seafloor (Figure 2). During this process, noble gases preferentially partition into the vapor phase, and the extent of noble gas loss from the melt is primarily controlled by initial melt CO_2 content and magmatic ascent rate (Figure 3). The two primary timescales governing volatile exsolution are those of decompression and diffusion. The decompression timescale, $t_{dec} = \Delta P / \frac{dP}{dt}$, represents the time it takes to decompress magma from the initial pressure to the final pressure, while the diffusion timescale $t_{diff} = L^2/D$ characterizes diffusive transfer around bubbles, where L is the half-distance between bubbles. We fix the initial bubble radius, such that higher magmatic CO_2 contents result in higher bubble number densities. The decompression time is scaled to the diffusion timescale of Ar, defining the dimensionless ascent parameter $\tau_{ascent} = t_{dec}/t_{diff}^{Ar}$. We utilize τ_{diff}^{Ar} to

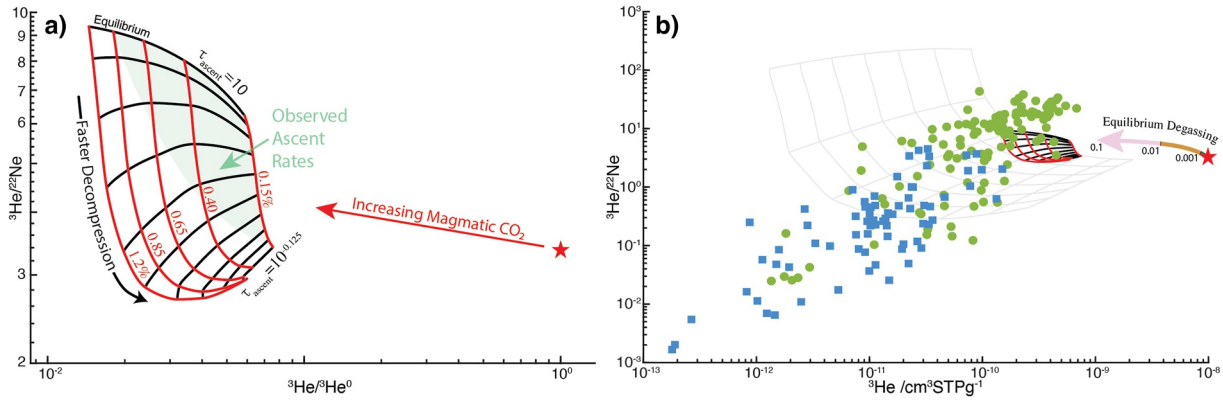

Figure 3. Model results for closed-system degassing (Stages 1 and 3) with a melt ascending from 1 to 0.5 kbar and an initial bubble radius of 10^{-5} m. (a) Red lines are magmatic CO_2 content contours, and black lines are contours of constant τ_{ascent}. As noble gases follow a partitioning relationship, ^3He is plotted as a ratio of its initial concentration in the melt. Magmatic CO_2 contents <0.15 wt.% are not shown. (b) Model results plotted against the global array of OIB (blue) and MORB (green) glasses. The 10-step degassing model of Gonnermann and Mukhopadhyay (2007) for an eruption depth of 3,500 m below sea level is plotted for reference as a gray net. Our initial pre-degassing ^3He concentration and $^3He/^{22}Ne$ ratio is plotted as a red star. The colored arrow represents an illustrative equilibrium closed-system degassing trajectory, discretized into bins by vesicularity. The bin limits ($\phi = 10^{-3}$, 10^{-2}, and 10^{-1}) represent ^3He loss proportions of 8%, 47%, and 90% respectively, and ^{22}Ne loss proportions of 23%, 75%, and 97% respectively. Our results show significantly less fractionation than those of Gonnermann and Mukhopadhyay (2007). As a result, we determine closed-system degassing can explain scatter in ^3He—$^3He/^{22}Ne$ values, but not the primary trend.

facilitate direct comparison with the closed-system degassing models of Gonnermann and Mukhopadhyay (2007) and Weston et al. (2015).

For a fixed value of τ_{ascent}, higher initial CO_2 concentrations lead to greater ^3He and ^{22}Ne loss from the melt (black contours in Figure 3a). At $\tau_{ascent} = 10$, where degassing approaches equilibrium, solubility-based partitioning, 94% of ^3He is lost from the melt at 0.15 wt.% CO_2, increasing to 98.6% at 1.2 wt.% CO_2. In contrast, increasing the ascent rate at constant CO_2 (i.e., decreasing τ_{ascent}) reduces the extent of gas loss to the vapor phase (red curves in Figure 3). Along the 1.2 wt.% CO_2 contour, decreasing τ_{ascent} from 10^1 to $10^{-0.125}$ reduces the extent of ^3He loss by 76%.

Sufficiently rapid ascent rates also suppress the preferential vapor-melt partitioning of Ne relative to He, reducing the melt $^3He/^{22}Ne$ ratio below equilibrium values through kinetic disequilibrium. For example, at $\tau_{ascent} = 10^{-0.125}$ and 0.15 wt.% CO_2, the final $^3He/^{22}Ne$ ratio is 4.38, rather than its equilibrium value of 6.23. At 1.2 wt.% CO_2, the final $^3He/^{22}Ne$ ratio decreases to 2.95, below the equilibrium value of 9.37; rapid decompression can therefore yield $^3He/^{22}Ne$ ratios lower than the initial mantle value of 3.38. The decompression rate required to produce non-equilibrium $^3He/^{22}Ne$ ratios increases with increasing magmatic CO_2 contents (Figure S8 in Supporting Information S1). In the examples above, the decompression rate at 0.15 wt.% CO_2 is 4.38 bar s^{-1}, whereas at 1.2 wt.% CO_2 it increases to 81.1 bar s^{-1}. This latter rate exceeds those inferred from geophysical and geochemical observations, which typically fall below ~5 bar s^{-1} (M. Jones et al., 2018). The shaded region in Figure 3 highlights the subset of the solution space for which decompression rates are consistent with observed decompression rates. For all values of τ_{ascent} considered here, the trends between ^3He and $^3He/^{22}Ne$ at decompression rates <5 bar s^{-1} are less negative than correlations across the global MORB-OIB compilation (Figure 3b). For a fixed bubble size and distribution, increasing the extent of decompression at a constant decompression rate can increase the magnitude of kinetic fractionation at intermediate vesicularities, although this effect is minimized at high and low vesicularity (Figure S9 in Supporting Information S1). For a fixed initial vesicularity, bubble size is positively correlated with the inter-bubble distance; consequently, increasing bubble radius at a fixed magmatic CO_2 content reduces the ascent rate required to generate kinetic fractionation (Figure S10 in Supporting Information S1). Increasing the difference between D_{He} and D_{Ne} enhances disequilibrium at a given decompression rate (Figure S11 in Supporting Information S1), but still does not reproduce the basaltic ^3He-$^3He/^{22}Ne$ trend.

We compare our closed-system LBM model to a single degassing step in the Gonnermann and Mukhopadhyay (2007) model, which is equivalent to closed-system degassing. Using the diffusion coefficients adopted in that study, our model predicts a comparable but more restricted trend in ^3He and $^3He/^{22}Ne$ space (Figure S12a in Supporting Information S1). In contrast, when the diffusion coefficients from this study are applied, the Gonnermann and Mukhopadhyay (2007) model produces values approaching equilibrium, whereas our LBM model exhibits compositional disequilibrium (Figure S12b in Supporting Information S1).

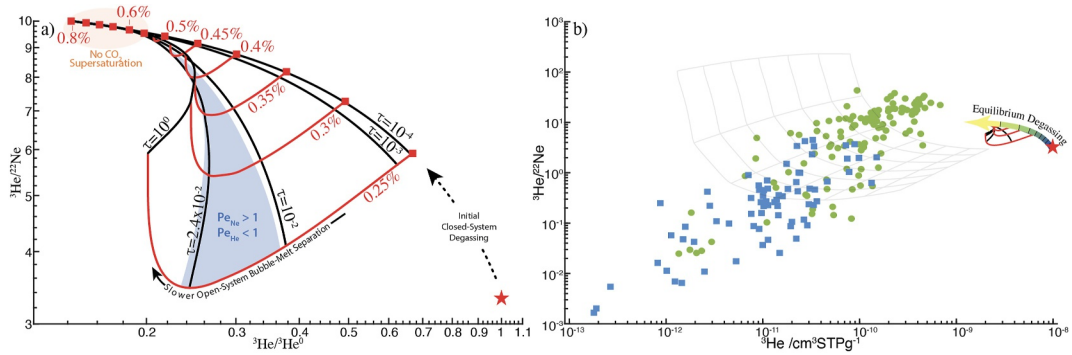

Figure 4. (a) Model results for open-system degassing at 1 kbar, with melt ascent from 3 kbar. Red curves denote melt CO_2 content contours, and black curves denote contours of constant τ_{ascent}. The initial pre-degassing melt ^{3}He concentration and ^{3}He/^{22}Ne ratio is plotted as a red star. Red squares mark the melt ^{3}He concentration and ^{3}He/^{22}Ne ratio at the start of open system degassing, following an initial stage of closed-system degassing during ascent of magma to the magma reservoir. At CO_2 contents below ∼0.2 wt.%, bubbles do not nucleate at 3 kbar, precluding gas loss because bubble nucleation during magmatic ascent is not considered. As noble gases follow a partitioning relationship, ^{3}He abundances are expressed as a ratio of their initial concentration in the melt. (b) Model results compared with the global array of OIB (blue squares) and MORB (green circles) glasses, and the model results of Gonnermann and Mukhopadhyay (2007) (gray net). The colored arrow illustrates an equilibrium closed-system degassing trajectory at 500 bar, discretized into 10% increments of cumulative CO_2 loss from the melt, spanning 0%–10% through to >90%.

3.2. The Effects of Open-System Degassing

Under conditions where bubbles rise through a stagnant magma reservoir (Stage 2, Figure 2), volatile mass is not conserved within a given melt parcel, and degassing proceeds as an open-system process. We assume that bubbles nucleate at depth below the magma reservoir, ascend to the reservoir coupled to their surrounding melt parcel, and decouple from the melt once the melt stagnates within the reservoir. For disequilibrium fractionation of noble gases to occur during the open-system stage, the melt must be CO_2-oversaturated upon entry into the magma reservoir. If instead the melt is at equilibrium with respect to CO_2 at the reservoir pressure, no additional bubble growth occurs during equilibration; vapor-phase noble-gas mole fractions remain unchanged, and no chemical potential gradients are generated to drive diffusion (this "No CO_2 Supersaturation" region is shaded in red in Figure 4a).

Within our LBM model, CO_2 supersaturation in the melt only develops at low total CO_2 contents—for example, below ∼0.5 wt.% at an ascent rate of 0.05 bar s^{-1} (Figure S13 in Supporting Information S1). Increasing the magmatic ascent rate shifts the development of CO_2 disequilibrium to higher CO_2 concentrations. When CO_2 supersaturation does develop during ascent, the subsequent bubble-melt CO_2 equilibration step reduces the mole fraction of noble gases within the bubble. Noble gas loss to the bubble is then governed by the bubble ascent timescale $t_{ascent} = H/U_b$ and the diffusion timescale $t_{diff} = L^2/D$. We scale the ascent timescale to the diffusion timescale of Ar to form $\tau_{ascent} = t_{ascent}/t_{diff}^{Ar}$, contours of which are shown with black lines in 4. In the limit of instantaneous bubble escape $(\tau_{ascent} \to 0)$, melt ^{3}He/^{22}Ne ratios remain near their initial solubility-controlled (pre-bubble expansion) values. Conversely, if bubbles do not move relative to the melt $(\tau_{ascent} \to \infty)$ melt-vapor equilibration becomes complete. In this equilibrium regime, ^{3}He loss exceeds that predicted by closed-system equilibrium due to dilution by growing bubbles, but the resulting ^{3}He/^{22}Ne ratio is the same as that at equilibrium. At intermediate values of τ_{ascent}, enough time is allowed for bubble-melt separation, but Ne diffusion is more kinetically limited than He diffusion, resulting in He-Ne fractionation. This effect is maximized when the ratio of advective to diffusive flux (i.e., the Péclet number, Equation 15) is given by $Pe_{He} < 1$ and $Pe_{Ne} > 1$ (blue shaded region in Figure 4a). The magnitude of this effect increases with decreasing total CO_2 content, reflecting increasing bubble spacing L. Bubble radius controls both t_{ascent} and the Péclet number through their dependence on bubble velocity (Equation 13), and we find that fractionation is maximized for bubbles with a radius between 10^{-5} m and 10^{-4} m.

No value of τ_{ascent} reproduces the trends observed in the global MORB-OIB compilation in ^{3}He-^{3}He/^{22}Ne space (Figure 4). The magnitude of ^{3}He loss is also insufficient to span the range exhibited by OIB and MORB.

Although the diffusion coefficients of He and Ne are subject to significant uncertainty (Amalberti et al., 2018), even adopting the highest published values of D_{He} and the lowest values of D_{Ne} (shown in Figure S4 in Supporting Information S1) fails to significantly reduce $^3He/^{22}Ne$ ratios (Figure S14 in Supporting Information S1). In the absence of an initial closed-system degassing stage that accounts for bubble growth history, our results align with those of Gonnermann and Mukhopadhyay (2007), even when a reduced diffusion coefficient contrast is utilized (Figure S15 in Supporting Information S1). However, incorporating this growth history is physically necessary, as discussed in Section 2.2.1.

4. Discussion

The results presented here show that open- and closed-system degassing yield distinct trends in the evolution of $^3He/^{22}Ne$ ratios and ^3He loss from melt to vapor, and that these trends can diverge from those predicted by equilibrium, solubility-based partitioning. We interpret these findings in the context of two mantle-source models:

1. A "Steady State" mantle with homogenous pre-degassing $^3He/^{22}Ne$ ratios in MORB and OIB sources.
2. Disequilibrium degassing as a solution to the so-called "Helium Paradox".

4.1. Closed-System Degassing Imposes Limits on Fractionation

In a closed system, noble-gas partitioning between melt and vapor is governed by the competition between decompression (ascent) and diffusion. Decompression alters the intrinsic thermodynamic state variables of the system, and when the rate of pressure change exceeds the rate at which diffusion can relax chemical potential gradients, disequilibrium fractionation develops.

During ascent of magma to a magma reservoir (Stage 1), the ascent rates inferred from geophysical and geochemical constraints (~0.002–0.1 m s^{-1} (Ma et al., 2024; Mutch et al., 2019)) are below those required to induce disequilibrium fractionation between ^3He and ^{22}Ne (≥1 m s^{-1}). Although CO_2 may exhibit measurable disequilibrium near the upper end of this range, He and Ne distribute between melt and vapor according to their equilibrium partition coefficients.

Ascent from a melt reservoir to the seafloor (Stage 3) is more rapid; effusive eruptions have been constrained at up to 1.2 m s^{-1} (Chavrit et al., 2012; Gardner et al., 2016; M. Jones et al., 2018; Paonita & Martelli, 2006; Soule et al., 2012). Even at these decompression rates, the diffusion lengths of He and Ne accumulated over decompression exceed the spacing between bubbles (Figure 5c). Thus, equilibrium partitioning dominates, and MORB and OIB closely follow equilibrium degassing pathways. At higher decompression rates characteristic of a transition toward Hawaiian activity (~10 m s^{-1}; Paonita and Martelli (2006), Burnard (1999)), non-equilibrium fractionation effects become more attainable, as He may locally equilibrate while Ne remains diffusion-limited (Figure 5b). However, increasing the decompression rate reduces the integrated time of kinetic fractionation, such that diffusion lengths for He and Ne remain small relative to the bubble spacing; diffusive loss to the vapor phase is therefore limited, and the impact of disequilibrium on mass balance is reduced (Figure 5a). Consequently, closed-system degassing alone does not result in significant fractionation between ^3He and ^{22}Ne, nor does it allow for OIB and MORB sources to be characterized by homogeneous pre-degassing $^3He/^{22}Ne$ ratios.

For disequilibrium degassing to resolve the "Helium Paradox," two constraints must hold:

(a) OIB melts begin with higher initial ^3He concentrations than MORB melts yet end with lower ^3He after ascent and degassing (Gonnermann & Mukhopadhyay, 2007).
(b) During this degassing the $^3He/^{22}Ne$ ratio of OIBs cannot exceed that of MORBs, despite greater ^3He loss.

Constraint (a) is plausible, as OIBs are often more volatile-enriched than MORBs (Dasgupta & Aubaud, 2024). Greater magmatic CO_2 contents correspond to a greater mass of exsolved CO_2 at a given pressure, and thus to a greater extent of ^3He loss from the melt to the vapor phase. Constraint (b) imposes a stricter requirement. At a given pressure, increasing magmatic CO_2 contents increases the mass of the exsolved vapor phase and, for a given bubble radius, increases bubble number density. Because bubble number density scales as $n_b \propto \phi / R_b^3$, the mean inter-bubble spacing decreases as $L \propto n_b^{-1/3}$, and inter-bubble length scales are reduced. Shorter inter-bubble lengths promote equilibration of He and Ne (Fick, 1855). OIB melts with elevated CO_2 contents thus require

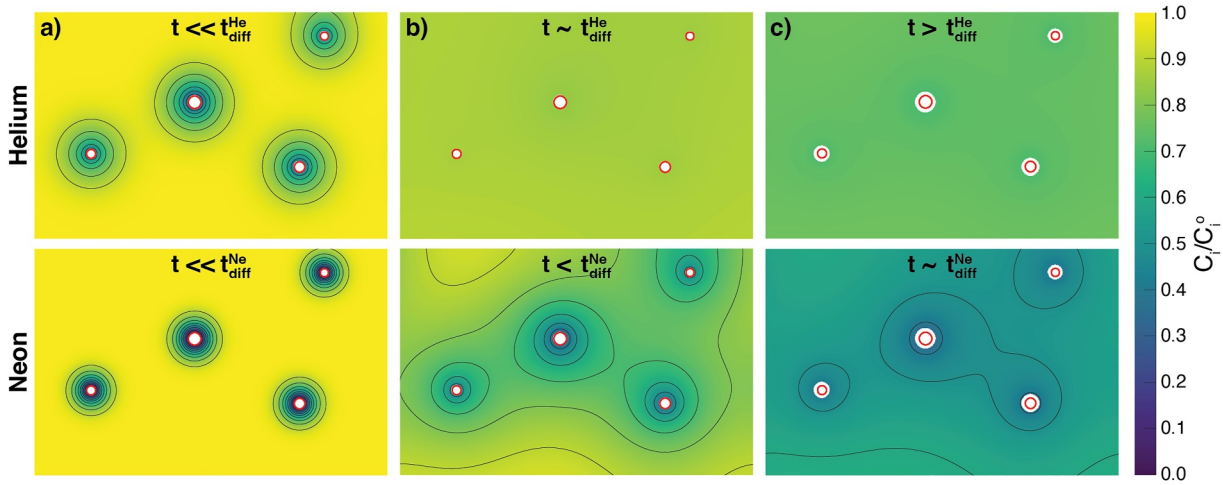

Figure 5. Spatial distributions of He (top row) and Ne (bottom row) concentrations normalized to their initial values in the melt $\left(C_i/C_i^0\right)$ around randomly distributed bubbles during magmatic ascent. The columns represent three time slices (a–c) during magmatic ascent, with time progressing from left to right. The timescale of He diffusion $\left(t_{\text{diff}}^{\text{He}}\right)$ is shorter than that of Ne diffusion $\left(t_{\text{diff}}^{\text{Ne}}\right)$. Iso-concentration lines are depicted in black, and initial bubble boundaries are shown in red. This panel demonstrates that the framework can resolve poly-disperse bubble size distributions. However, the analyses reported in the results use a single-bubble domain. The periodic boundary conditions render the single-bubble domain equivalent to a unit cell of an infinite periodic array, capturing first-order inter-bubble effects. This approach enables us to reduce parameter dimensionality and derive insight into noble gas distributions during degassing whilst limiting complexity. We also note that at low bubble fractions there is insignificant interaction between bubbles.

more rapid decompression than MORB melts in order for non-equilibrium degassing to prevent a ^{3}He/^{22}Ne increase through degassing. Considering these constraints, systematic differences in either decompression rates or bubble populations between OIB and MORB melts are required for disequilibrium degassing to resolve the "Helium Paradox."

When evaluated against available observations of decompression rates and bubble distributions, these requirements are not supported by any systematic differences between OIB and MORB melts. Reported decompression rates show, at most, a weak positive correlation with CO_2 contents (Chavrit et al., 2012; Geiger et al., 2025; Mutch et al., 2019; Neave & Maclennan, 2020), insufficient to maintain disequilibrium at increased CO_2 concentrations. Similarly, there are no systematic trends in bubble size distributions between OIB and MORB glasses that could produce sufficiently diverging degassing pathways (Dasgupta & Aubaud, 2024; J. G. Jones, 1969; M. Jones et al., 2020), although we note that this data is not comprehensive. Finally, deeper bubble nucleation resulting from higher volatile contents (Shea, 2017) does not compensate for the shorter diffusive length scales resulting from higher magmatic CO_2 contents. Taken together, these constraints imply that systematic differences in closed-system degassing pathways between OIB and MORB melts are insufficient to generate disequilibrium effects capable of resolving the "Helium Paradox."

In finding that a single stage of closed-system degassing cannot reproduce the full range of ^{3}He concentrations and ^{3}He/^{22}Ne ratios in the global array (Figure 1), our results are broadly consistent with those of Gonnermann and Mukhopadhyay (2007), Weston et al. (2015), and Tucker et al. (2018). We suggest that closed-system disequilibrium degassing may result in only slight scatter in measured ^{3}He/^{22}Ne ratios, and this signal is overwhelmed by factors including contamination and uncertainty on solubility coefficients when determining ^{3}He/^{22}Ne ratios in pre-degassing mantle sources (Yamamoto & Kurz, 2022). Additionally, absolute He concentrations in basaltic glasses are notoriously unreliable due in part to the effects of seawater and atmospheric contamination (Burnard et al., 2003; Stroncik & Niedermann, 2016), and the exact isotopic proxy used to screen for contaminated samples can substantially contract or expand the apparent global ^{3}He–^{3}He/^{22}Ne array (Figure S3 in Supporting Information S1). These considerations indicate that even the deliberately exaggerated disequilibrium effect produced by initializing our system with a pure CO_2 bubble devoid of noble gases is likely unresolvable within the current global sample suite.

4.2. Open-System Degassing Exhibits Limited Fractionation

When bubbles rise through a melt that is mostly at rest, such as within a magma reservoir, degassing behaves as an open system (Stage 2, Figure 2). In this stagnant melt, noble gas loss from the melt to the bubble is governed by the initial degree of melt–bubble disequilibrium inherited upon reservoir entry and by the relative rates of bubble ascent and noble gas diffusion within the melt.

We consider that, prior to Stage 2, bubbles nucleate at a depth below a magma reservoir, and ascend to it during Stage 1 at a rate of 0.05 bar s^{-1} (consistent with magmatic ascent rates beneath mid-ocean ridge systems; Ma et al. (2024)). As discussed, melt-bubble separation velocities are too low over the integrated time of ascent during Stage 1 to result in melt-bubble separation, and it can be treated as a closed system. Furthermore, as bubble decompression timescales (>hours; Coumans et al. (2020)) exceed the characteristic diffusion timescales of the system (~minutes), He and Ne partition according to their solubility coefficients during ascent (Section 4.1), and melt-bubble ^{3}He and ^{22}Ne concentrations are equilibrated upon entry into the magma reservoir. In contrast, as CO_2 diffuses more slowly, it may be oversaturated within the melt upon reservoir entry. Once bubbles are emplaced within the reservoir, we first distribute CO_2 between melt and vapor according to its solubility in the melt, and then treat the bubble as rising independently of the stalled melt. Under these open-system conditions, ^{3}He and ^{22}Ne concentrations in the melt may subsequently evolve through continued diffusive exchange with the ascending vapor phase.

We find that in melts with greater initial CO_2 contents, bubbles grow in near mechanical and chemical equilibrium with the system, such that growth is solubility-limited (Lensky et al., 2004). This finding is consistent with both experimental (Pichavant et al., 2013) and observational (D. W. R. Jones & Rudge, 2020) studies. As a result, bubbles in CO_2-rich melts experience only limited growth-imposed noble gas dilution upon emplacement in the magma reservoir, suppressing the bubble growth effect required to create a concentration gradient between the melt and the bubble interface. This suggests that although higher CO_2 contents increase the absolute magnitude of noble gas loss from the melt, $^{3}He/^{22}Ne$ ratios do not change appreciably during open-system degassing. Thus, greater degassing extents in more CO_2-rich OIB melts do not provide a viable resolution to the "Helium Paradox."

In contrast, in low-CO_2 melts, bubble number densities are lower (Soule et al., 2012), increasing the inter-bubble length scales over which CO_2 must diffuse to equilibrate between melt and bubbles. As a result, CO_2 diffusion length scales are insufficient to fully relax decompression-induced solubility decreases, and the melt is therefore supersaturated in CO_2 upon entry into the magma reservoir. Partitioning of CO_2 between melt and bubble is then able to drive bubble growth, reducing noble gas partial pressures within the bubble. This creates a chemical potential gradient that drives diffusive transfer of noble gases from the melt into the vapor phase during open-system degassing, potentially allowing for non-equilibrium effects to develop.

The extent to which ^{3}He and ^{22}Ne are then lost from the melt during open-system degassing following bubble growth depends on the efficiency with which bubbles extract and transport these elements out of the system. To provide a predictive framework for contextualizing our results and understanding whether noble gas transport is diffusion- or advection-controlled, we utilize the Péclet number (introduced in Equation 15). The Péclet number expresses the ratio of advective to diffusive flux over a characteristic length-scale L and, for a given melt-bubble separation velocity U_b, varies inversely with the element-specific diffusion coefficient D_i. Consequently, the Péclet number differs for He and Ne. At high melt-bubble separation velocities, we enter a regime characterized by $Pe_{He} \gg 1$ and $Pe_{Ne} \gg 1$. Here, diffusion of both He and Ne is transport-limited and the chemical composition of the bubble remains close to that established prior to ascent (i.e., the equilibrium state at P_0). Conversely, at low melt-bubble separation velocities where $Pe_{He} < 1$, and $Pe_{Ne} < 1$, diffusion timescales for He and Ne are shorter than the bubble ascent timescale. In this regime, K_i approaches the equilibrium partition coefficient for the diluted bubble, and ^{3}He and ^{22}Ne equilibrate efficiently between the melt and vapor phase. However, because initial bubble–melt compositions reflect equilibrium partitioning, this process does not modify the $^{3}He/^{22}Ne$ ratio of the melt.

Maximum fractionation occurs at intermediate melt-bubble separation velocities, characterized by $Pe_{He} > 1$ and $Pe_{Ne} < 1$. In this regime, He can approach equilibrium, but Ne loss to the bubble is kinetically limited owing to its lower diffusivity. We find that this regime corresponds to bubble radii within range of those recorded in MORB and OIB glasses at the sea floor (Burnard, 1999; Chavrit, 2010; Hawkins & Melchior, 1983; Shea et al., 2010; Soule et al., 2012; Staudacher et al., 1989; Voyer et al., 2015). This size correspondence could be taken to suggest

that kinetic fractionation could occur under natural conditions if bubbles rise within this size range. However, our model intentionally maximizes non-equilibrium effects through the assumption of instantaneous bubble expansion, and thus our results are upper bounds on the amount of fractionation that could occur. Modifying the model to include He and Ne diffusion during the bubble expansion stage prior to open system degassing would further limit kinetic fractionation effects, as bubble growth timescales are longer than diffusive timescales for all but the most rapid decompression rates (Coumans et al., 2020; B. Watson et al., 1982). Therefore, although open-system degassing can reduce melt ^{3}He and ^{22}Ne contents below those achievable under closed-system conditions, kinetic effects result in limited deviation from the ^{3}He/^{22}Ne ratios expected from equilibrium, partition-coefficient controlled degassing.

4.3. Fundamental Differences From Previous Models

Both Gonnermann and Mukhopadhyay (2007) and Weston et al. (2015) proposed that non-equilibrium degassing could resolve the Helium Paradox and allow MORB and OIB sources to share a common pre-degassing ^{3}He/^{22}Ne ratio. Although the trends between ^{3}He and ^{3}He/^{22}Ne in this contribution are overall comparable to these studies —particularly during closed-system degassing—the magnitude of fractionation is significantly reduced, and our results are more aligned with those of Tucker et al. (2018). Below, we explore how this fundamental discrepancy arises from key differences in model geometry, melt-bubble boundary conditions, degassing history, and the choice of physical parameters.

During our closed-system degassing stage, we treat the bubble as an infinite cylinder. In contrast, the degassing models of Gonnermann and Mukhopadhyay (2007), Weston et al. (2015), and Tucker et al. (2018) approximate the melt-bubble boundary as an infinite plane sheet, and quantify the extent of equilibrium using the solution of Crank (1975):

$$\theta = \frac{8}{\pi^2}\sum_{j=0}^{\infty}\frac{1}{(2j+1)^2}\exp\left[\frac{-D(2j+1)^2\pi^2 t_{\text{degas}}}{4L^2}\right]. \tag{17}$$

Here, $(1-\theta)$ represents the fraction of a species that diffuses across a melt-bubble boundary within a time t_{degas}. At early times, differences between the 2D and 1D geometries lead to measurable deviations between model results, reflecting the influence of bubble curvature. These discrepancies diminish with time, and both models ultimately exhibit convergent behavior for a fixed gas volume fraction. We further deviate from previous models in explicitly incorporating the effects of bubble growth during decompression. This results in a time-dependent, rather than fixed, boundary condition. Additionally, unlike Gonnermann and Mukhopadhyay (2007), we utilize a non-constant pressure during closed-degassing, making our approach more similar to that of Weston et al. (2015).

Additional differences arise from utilisation of different noble gas diffusion coefficients. Gonnermann and Mukhopadhyay (2007) and Weston et al. (2015) adopted values of $D_{\text{He}} = 10^{-8.3}$ m^2 s^{-1} and $D_{\text{Ne}} = 10^{-11.2}$ m^2 s^{-1}. Subsequent experimental work has suggested that the difference between He and Ne diffusion coefficients may be smaller, although these parameters remain poorly constrained and subject to considerable uncertainty (Amalberti et al., 2018; Guillot & Sator, 2012)). Following the approach of Tucker et al. (2018), we utilize $D_{\text{He}} = 10^{-8.5}$ and $D_{\text{Ne}} = 10^{-9}$ m^2 s^{-1}. These values reduce the magnitude of kinetic fractionation in the model of Gonnermann and Mukhopadhyay (2007) (Figure S16 in Supporting Information S1), and lead Tucker et al. (2018) to conclude that non-equilibrium degassing does not solve the "Helium Paradox." Crucially, however, our determination that non-equilibrium open-system degassing does not solve the "Helium Paradox" is not dependent on precise knowledge of (poorly defined) He and Ne diffusion coefficients.

Our approach differs from previous studies in that we impose an initial closed-system bubble growth stage before open-system degassing, which places a fundamental upper limit on the magnitude of fractionation achievable during subsequent open-system behavior, even for large contrasts between D_{He} and D_{Ne}. A closed-system degassing step is physically unavoidable, as small bubbles exhibit extremely low hindered Hadamard–Rybczynski upwelling velocities (Faroughi & Huber, 2015), preventing immediate decoupling from the melt. During this closed-system stage, bubble-growth timescales are significantly greater than noble gas diffusion timescales, resulting in near-equilibrium noble gas partitioning. This initial equilibrium distribution moderates subsequent kinetic effects, even when we exaggerate the effects of open-system degassing by treating bubble

growth within the magma reservoir as instantaneous. We note that we did not explicitly consider alternative bubble nucleation and growth scenarios (e.g., CO_2 flushing; Caricchi et al. (2018)), but expect them to have a similar effect on initial noble gas distributions between melt and vapor, even if the exact relationship between CO_2 content and noble-gas dilution through bubble growth differs.

A final discrepancy lies in how open-system behavior is approximated. Gonnermann and Mukhopadhyay (2007) and Weston et al. (2015) treat open-system degassing as a series of discrete events: bubble nucleation and instantaneous growth, diffusive exchange for a fixed time, and instantaneous bubble removal. Tucker et al. (2018) extend this framework to a continuous process. These formulations do not consider the finite ascent rate of bubbles, and by assuming that melt concentration gradients are fully relaxed to a homogeneous state prior to each nucleation event, they impose a sharp concentration boundary at the melt-bubble interface which enhances diffusive transport. In contrast, we utilize a 1D coupled diffusion-advection approach to investigate the effects of finite bubble escape velocities. When this modification is applied in isolation—excluding an equilibrium closed-system stage—our results define a similar trend to the multi-step models of Gonnermann and Mukhopadhyay (2007) and Weston et al. (2015), even when using the diffusion coefficient values of Tucker et al. (2018). This underscores the importance of considering bubble growth history controls on the magnitude of kinetic fractionation produced during open-system degassing.

4.4. Implications for the Interpretation of Mantle Sources

We modeled the kinetic controls on He and Ne fractionation during open- and closed-system degassing and determined that under both regimes, ^{3}He concentrations and ^{3}He/^{22}Ne ratios closely follow equilibrium degassing pathways.

A natural extension of these results is that non-equilibrium degassing alone cannot reproduce global trends between ^{3}He concentrations and ^{3}He/^{22}Ne, and therefore cannot resolve the "Helium Paradox." This conclusion is consistent with studies suggesting that the low ^{4}He/^{3}He ratios observed in many OIBs do not require the preservation of some undegassed fraction of a "primordial" lower-mantle reservoir (Parai, 2024; Stracke et al., 2022), and that the plume mantle source is a heterogeneous mixture of primordial and recycled components (Parai et al., 2019). It also aligns with a framework in which plume sources plume source are low in both radiogenic ^{4}He and primordial ^{3}He, resulting in low ^{4}He/^{3}He ratios accompanied by low absolute helium concentrations (Dygert et al., 2018; Gonnermann & Mukhopadhyay, 2009; M. G. Jackson et al., 2021; Parman, 2007; Wang et al., 2022).

An alternative mechanism to resolve noble gas signatures in OIBs invokes compositional modification by core-derived components. Emerging evidence suggests that He—and possibly H and ^{182}W—isotope systematics in plumes may reflect core–mantle exchange (Bouhifd et al., 2020; Dottin et al., 2025; Horton et al., 2023; Mundl-Petermeier et al., 2020; Olson & Sharp, 2022; Porcelli & Halliday, 2001). In this framework, depleted mantle material is overprinted by helium from the core, which exhibits low ^{4}He/^{3}He ratios acquired through nebular-gas ingassing and/or early core formation (Deng et al., 2023), potentially generating OIB source regions with low ^{4}He/^{3}He ratios and low absolute helium abundances. However, this hypothesis faces significant geochemical constraints. A core contribution would require comparatively large ^{3}He fluxes (600–800 mol year^{-1}; Olson and Sharp (2022)), while ab initio partitioning calculations predicts core ^{3}He/^{22}Ne ratios of order 10^3, exceeding those observed in OIBs (Li et al., 2022). Moreover, the full mantle noble-gas array (He, Ne, Ar, Kr, Xe) is not readily explained by diffusive transport from the core (Parai, 2024). Thus, if core-derived helium is to resolve the "Helium Paradox," a mechanism is required to re-fractionate noble gases and transport them across the core–mantle boundary (e.g., Deng et al. (2023)).

Because ^{3}He concentrations and ^{3}He/^{22}Ne ratios deviate little from equilibrium during degassing, ^{3}He and ^{22}Ne contents of MORB and OIB must primarily reflect source heterogeneity rather than non-equilibrium degassing. In this context, our approach provides a mechanistic understanding for the conclusion of Parai et al. (2019): that plume and MORB noble-gas isotope arrays cannot be reproduced by kinetic fractionation of a single starting reservoir. Our requirement for source heterogeneity is not contradicted by geochemical evidence suggesting that ^{3}He/^{22}Ne ratios span from ~2 to $\gtrsim$10 across MORB and OIB sources (Coltice et al., 2011; Graham, 2002; Kurz et al., 2009; Péron et al., 2016; Raquin & Moreira, 2009; Tucker et al., 2018; Yamamoto & Kurz, 2022; X. J. Zhang et al., 2024), with values intermediate between plumes and depleted MORBs attributed to mixing between MORB and plume sources (Tucker & Mukhopadhyay, 2014).

4.5. Model Limitations

In the absence of well-constrained He and Ne diffusion coefficients, we must place severe constraints on any modeling work that seeks to utilize He and Ne diffusion coefficients to understand Earth system processes. Molecular dynamics simulations and experimental studies suggest that He and Ne diffusion coefficients in basaltic melts at magmatic temperatures differ by less than an order of magnitude. However, although studies indicate that melt polymerization, viscosity, volatile contents, and network modifying cations (e.g., Fe, Ca, Na) influence diffusion, the relative importance of these parameters on noble gas diffusion in melts has not been constrained (Y. Zhang & Gan, 2022). Until diffusion coefficients are better defined, we can assess whether noble gas diffusion kinetics exert a first-order control on observed systematics, but we cannot quantify the specific influence on individual samples. Importantly, none of our conclusions depend on precise knowledge of He and Ne diffusion coefficients. Improved constraints would instead be most relevant for heavier noble gases, such as Ar, which diffuse at rates comparable to or slower than CO_2 (Nowak et al., 2004).

We do not incorporate H_2O within our bubble growth model due to its low contribution to bubble growth relative to CO_2 at the pressures of interest. However, if the effects of melt CO_2 and H_2O contents on noble gas diffusion coefficients could be defined, it would further justify an expansion of our pure-CO_2 approach to include H_2O, and for water-dependent melt viscosity and noble gas diffusivity to be taken into account. This would be possible, as the relaxation times for the discrete Boltzmann equations that represent momentum and mass conservation can be varied locally.

Effusively erupting basalts primarily degas through gas exsolution into pre-existing bubbles (M. Jones et al., 2018), rather than via secondary nucleation. Accordingly, we initialize our LBM simulations with pre-existing bubbles and model their subsequent growth, excluding secondary nucleation events. However, at high decompression rates, secondary nucleation is expected to occur, increasing the bubble number density of the melt (Toramaru, 2014), and thereby mitigating kinetic fractionation effects. Our LBM framework is readily extensible to accommodate secondary nucleation, and future work could explore its influence on disequilibrium. Additionally, while we model a single bubble, incorporating a distribution of bubble sizes would allow for evaluation of the relative contributions of large and small bubbles to measured noble gas signatures. This may be relevant for step crushing analyses—in which we may expect progressively smaller bubbles to release their noble gas contents (Núñez-Guerrero et al., 2025)—and for bubble-resolved analyses of volcanic glasses (e.g., Burnard, 1999).

A key finding in this work is that imposing an equilibrium pre-degassing step prior to bubble expansion and melt–bubble separation substantially reduces the range of ^{3}He concentrations and ^{3}He/^{22}Ne ratios produced through open-system degassing. Explicitly accounting for the timescale of CO_2 diffusion during bubble growth would further suppress the development of disequilibrium, as CO_2 diffuses more slowly than He and Ne (Aubry et al., 2013). This additional drive toward equilibrium would work to reinforce our conclusion that non-equilibrium degassing is not a primary control on noble gas concentrations in basaltic samples.

5. Conclusions

Closed-system degassing—such as during magmatic ascent to a sub-volcanic reservoir or to the seafloor—produces only limited disequilibrium effects in ^{3}He -^{3}He/^{22}Ne space because diffusion timescales are short relative to decompression timescales. Disequilibrium effects are likewise limited during open-system degassing, as vapor bubbles remain in diffusive equilibrium with their surrounding melt until they grow sufficiently large to decouple. As a result, an initial near-equilibrium closed-system stage limits the magnitude of kinetic fractionation that can be achieved during subsequent open-system degassing. A further consequence of this is that the limited capacity of magmatic degassing to follow non-equilibrium pathways is largely insensitive to uncertainties in D_{He} and D_{Ne} over their experimentally constrained ranges.

We therefore argue that disequilibrium degassing of ^{3}He and ^{22}Ne does not exert a primary control on global correlations between ^{3}He concentrations and ^{3}He/^{22}Ne ratios in MORB and OIB glasses. Consequently, non-equilibrium degassing does not resolve the so-called "Helium Paradox," and thus does not provide a mechanism to reconcile low ^{4}He/^{3}He ratios in some OIBs with the presence of a less-degassed, "primordial" lower-mantle reservoir. More broadly, our results indicate that MORB–OIB differences in ^{3}He/^{22}Ne must arise from source heterogeneity rather than from degassing processes.

Acronyms

MORB	Mid-Ocean Ridge Basalt
OIB	Ocean Island Basalt
LBM	Lattice Boltzmann Method

Notation

U_b	Bubble Velocity
U_m	Melt Velocity
ν	Kinematic Viscosity
D_i	Diffusion Coefficient of Volatile i
c_s	Lattice Speed of Sound
ρ	Fluid Density
n	Moles of Gas Molecules
R	Ideal Gas Constant
V	Volume
T	Temperature
P	Pressure
g	Gravitational Constant
K	Partition Coefficient
K_H	Henry's Law Solubility Coefficient
ϵ_H	Henry's Law Solubility Exponent
R_b	Bubble Radius
M	Mass Ratio Between Vapor and Melt
L	Length Scale for Diffusion
κ	Curvature of Gas-Melt Interface
Π	Disjoining Pressure
ξ	Particle Velocity Space
χ_i	Mole Fraction of Species i
t	Time
μ	Dynamic Viscosity
w_i	Lattice Weights in LBM Model
σ	Surface Tension
τ	Relaxation Time in LBM Model
$\mathbf{e_i}$	Lattice Velocity in i Direction of LBM Model
f_i	Distribution Function in i Direction of D2Q9 Model
g_i	Distribution Function in i Direction of D2Q5 Model for CO_2
h_i	Distribution Function in i Direction of D2Q5 Model for Noble Gases

F_i	Body Force in i Direction on f_i
C_i	Concentration of Volatile i
ϕ	Vesicularity
Pe	Péclet number

Conflict of Interest

The authors declare no conflicts of interest relevant to this study.

Availability Statement

The C++ and MATLAB codes used to create our Lattice Boltzmann Model and coupled 1D open-system degassing model are available via the Brown Digital Repository at https://doi.org/10.26300/j4ra-xe88.

Acknowledgments
This work was supported by the LunaSCOPE NASA SSERVI node (Grant 80NSSC23M0161). We thank E. Attar and C. Körner for allowing us to obtain a copy of their LB model.

References

Albarède, F. (2008). Rogue mantle helium and neon. *Science*, *319*(5865), 943–945. https://doi.org/10.1126/science.1150060

Allègre, C. J., Staudacher, T., Sarda, P., & Kurz, M. (1983). Constraints on evolution of Earth's mantle from rare gas systematics. *Nature*, *303*(5920), 762–766. https://doi.org/10.1038/303762a0

Amalberti, J., Burnard, P., Tissandier, L., & Laporte, D. (2018). The diffusion coefficients of noble gases (He–Ar) in a synthetic basaltic liquid: One-dimensional diffusion experiments. *Chemical Geology*, *480*, 35–43. https://doi.org/10.1016/j.chemgeo.2017.05.017

Anderson, D. L. (1998). The helium paradoxes. *Proceedings of the National Academy of Sciences*, *95*(9), 4822–4827. https://doi.org/10.1073/pnas.95.9.4822

Arnulf, A., Harding, A., Kent, G., Carbotte, S., Canales, J., & Nedimović, M. (2014). Anatomy of an active submarine volcano. *Geology*, *42*(8), 655–658. https://doi.org/10.1130/g35629.1

Aubaud, C., Pineau, F., Jambon, A., & Javoy, M. (2004). Kinetic disequilibrium of C, He, Ar and carbon isotopes during degassing of mid-ocean ridge basalts. *Earth and Planetary Science Letters*, *222*(2), 391–406. https://doi.org/10.1016/j.epsl.2004.03.001

Aubry, G. J., Sator, N., & Guillot, B. (2013). Vesicularity, bubble formation and noble gas fractionation during MORB degassing. *Chemical Geology*, *343*, 85–98. https://doi.org/10.1016/j.chemgeo.2013.02.006

Bamber, E. C., Spina, G. L., Arzilli, F., Polacci, M., Mancini, L., Vitturi, M. D. M., et al. (2024). Outgassing behaviour during highly explosive basaltic eruptions. *Communications Earth & Environment*, *5*(1), 3. https://doi.org/10.1038/s43247-023-01182-w

Behrens, H. (2010). Noble gas diffusion in silicate glasses and melts. *Reviews in Mineralogy and Geochemistry*, *72*(1), 227–267. https://doi.org/10.2138/rmg.2010.72.6

Bhatnagar, P. L., Gross, E. P., & Krook, M. (1954). A model for collision processes in gases I. Small amplitude processes in charged and neutral one-component systems. *Physical Review*, *94*(3), 511–525. https://doi.org/10.1103/physrev.94.511

Bouhifd, A. M., Jephcoat, A. P., Porcelli, D., Kelley, S. P., & Marty, B. (2020). Potential of Earth's core as a reservoir for noble gases: Case for helium and neon. *Geochemical Perspectives Letters*, 15–18. https://doi.org/10.7185/geochemlet.2028

Burnard, P. (1999). Eruption dynamics of "popping rock" from vesicle morphologies. *Journal of Volcanology and Geothermal Research*, *92*(3–4), 247–258. https://doi.org/10.1016/s0377-0273(99)00057-8

Burnard, P., Harrison, D., Turner, G., & Nesbitt, R. (2003). Degassing and contamination of noble gases in mid-Atlantic ridge basalts. *Geochemistry, Geophysics, Geosystems*, *4*(1), 1–20. https://doi.org/10.1029/2002gc000326

Carbotte, S. M., Marjanović, M., Arnulf, A. F., Nedimović, M. R., Canales, J. P., & Arnoux, G. M. (2021). Stacked magma lenses beneath mid-ocean ridges: Insights from new seismic observations and synthesis with prior geophysical and geologic findings. *Journal of Geophysical Research: Solid Earth*, *126*(4), e2020JB021434. https://doi.org/10.1029/2020jb021434

Caricchi, L., Sheldrake, T. E., & Blundy, J. (2018). Modulation of magmatic processes by CO_2 flushing. *Earth and Planetary Science Letters*, *491*, 160–171. https://doi.org/10.1016/j.epsl.2018.03.042

Chavrit, D. (2010). *Cartographie globale des flux de CO2 à l'axe des dorsales océaniques* (Unpublished doctoral dissertation). Université de Nantes.

Chavrit, D., Humler, E., Morizet, Y., & Laporte, D. (2012). Influence of magma ascent rate on carbon dioxide degassing at oceanic ridges: Message in a bubble. *Earth and Planetary Science Letters*, *357*, 376–385. https://doi.org/10.1016/j.epsl.2012.09.042

Coltice, N., Moreira, M., Hernlund, J., & Labrosse, S. (2011). Crystallization of a basal magma ocean recorded by helium and neon. *Earth and Planetary Science Letters*, *308*(1–2), 193–199. https://doi.org/10.1016/j.epsl.2011.05.045

Coumans, J., Llewellin, E., Wadsworth, F., Humphreys, M., Mathias, S., Yelverton, B., & Gardner, J. (2020). An experimentally validated numerical model for bubble growth in magma. *Journal of Volcanology and Geothermal Research*, *402*, 107002. https://doi.org/10.1016/j.jvolgeores.2020.107002

Crank, J. (1975). *The mathematics of diffusion*. Oxford University Press.

Dasgupta, R., & Aubaud, C. (2024). Major volatiles in the earth's mantle beneath mid-ocean ridges and intraplate ocean islands. In *Treatise on geochemistry*. Elsevier. Retrieved from https://hal.science/hal-04730561v1

Deng, Z., Schiller, M., Jackson, M. G., Millet, M.-A., Pan, L., Nikolajsen, K., et al. (2023). Earth's evolving geodynamic regime recorded by titanium isotopes. *Nature*, *621*(7977), 100–104. https://doi.org/10.1038/s41586-023-06304-0

Dixon, J. E. (1997). Degassing of alkalic basalts. *American Mineralogist*, *82*(3–4), 368–378. https://doi.org/10.2138/am-1997-3-415

Dottin, J. W. I., Horton, F., Alexander, C. M. O., Shahar, A., Wang, J., Boesenberg, J. S., et al. (2025). Hydrogen isotopic evidence for a core component in Baffin Island lavas. *Science Advances*, *11*(17), eadr2917. https://doi.org/10.1126/sciadv.adr2917

Duan, Z., & Zhang, Z. (2006). Equation of state of the H_2O, CO_2, and H_2O–CO_2 systems up to 10 GPa and 2573.15 K: Molecular dynamics simulations with ab initio potential surface. *Geochimica et Cosmochimica Acta*, *70*(9), 2311–2324. https://doi.org/10.1016/j.gca.2006.02.009

Dygert, N., Jackson, C. R., Hesse, M. A., Tremblay, M. M., Shuster, D. L., & Gu, J. T. (2018). Plate tectonic cycling modulates Earth's 3He/22Ne ratio. *Earth and Planetary Science Letters*, *498*, 309–321. https://doi.org/10.1016/j.epsl.2018.06.044

Faroughi, S. A., & Huber, C. (2015). Unifying the relative hindered velocity in suspensions and emulsions of nondeformable particles. *Geophysical Research Letters*, *42*(1), 53–59. https://doi.org/10.1002/2014gl062570

Fick, A. (1855). Ueber diffusion. *Annalen der Physik*, *170*(1), 59–86. https://doi.org/10.1002/andp.18551700105

Gardner, J., Jackson, B., Gonnermann, H., & Soule, S. (2016). Rapid ascent and emplacement of basaltic lava during the 2005–06 eruption of the East Pacific rise at ca. 9°51′N as inferred from CO_2 contents. *Earth and Planetary Science Letters*, *453*, 152–160. https://doi.org/10.1016/j.epsl.2016.08.007

Geiger, H., Weis, F., Troll, V. R., Deegan, F. M., Skogby, H., & Carracedo, J. C. (2025). Explosive ocean island volcanism explained by high magmatic water content determined through nominally anhydrous minerals. *Geochemistry, Geophysics, Geosystems*, *26*(2), e2024GC012013. https://doi.org/10.1029/2024gc012013

Giordano, D., Russell, J. K., & Dingwell, D. B. (2008). Viscosity of magmatic liquids: A model. *Earth and Planetary Science Letters*, *271*(1–4), 123–134. https://doi.org/10.1016/j.epsl.2008.03.038

Gonnermann, H. M., & Mukhopadhyay, S. (2007). Non-equilibrium degassing and a primordial source for helium in ocean-island volcanism. *Nature*, *449*(7165), 1037–1040. https://doi.org/10.1038/nature06240

Gonnermann, H. M., & Mukhopadhyay, S. (2009). Preserving noble gases in a convecting mantle. *Nature*, *459*(7246), 560–563. https://doi.org/10.1038/nature08018

Graham, D. W. (2002). Noble gas isotope geochemistry of mid-ocean ridge and ocean island basalts: Characterization of mantle source reservoirs. *Reviews in Mineralogy and Geochemistry*, *47*(1), 247–317. https://doi.org/10.2138/rmg.2002.47.8

Guillot, B., & Sator, N. (2012). Noble gases in high-pressure silicate liquids: A computer simulation study. *Geochimica et Cosmochimica Acta*, *80*, 51–69. https://doi.org/10.1016/j.gca.2011.11.040

Gülcher, A. J. P., Ballmer, M. D., & Tackley, P. J. (2021). Coupled dynamics and evolution of primordial and recycled heterogeneity in Earth's lower mantle. *Solid Earth*, *12*(9), 2087–2107. https://doi.org/10.5194/se-12-2087-2021

Hadamard, J. (1911). Mouvement permanent lent d'une sphère liquide et visqueuse dans un liquide visqueux. *Comptes Rendus de l'Académie des Sciences*, *152*, 1735–1752.

Hawkins, J., & Melchior, J. (1983). Petrology of basalts from Loihi seamount, Hawaii. *Earth and Planetary Science Letters*, *66*, 356–368. https://doi.org/10.1016/0012-821x(83)90151-6

Hilton, D., & Porcelli, D. (2014). 3.8—Noble gases as tracers of mantle processes. In H. D. Holland & K. K. Turekian (Eds.), *Treatise on geochemistry* (2nd ed., pp. 327–353). Elsevier. https://doi.org/10.1016/B978-0-08-095975-7.00206-0

Honda, M., McDougall, I., Patterson, D. B., Doulgeris, A., & Clague, D. A. (1993). Noble gases in submarine pillow basalt glasses from Loihi and Kilauea, Hawaii: A solar component in the Earth. *Geochimica et Cosmochimica Acta*, *57*(4), 859–874. https://doi.org/10.1016/0016-7037(93)90174-u

Horton, F., Asimow, P. D., Farley, K. A., Curtice, J., Kurz, M. D., Blusztajn, J., et al. (2023). Highest terrestrial 3He/4He credibly from the core. *Nature*, *623*(7985), 90–94. https://doi.org/10.1038/s41586-023-06590-8

Huber, C., Bachmann, O., Vigneresse, J., Dufek, J., & Parmigiani, A. (2012). A physical model for metal extraction and transport in shallow magmatic systems. *Geochemistry, Geophysics, Geosystems*, *13*(8). https://doi.org/10.1029/2012gc004042

Huber, C., Su, Y., Nguyen, C. T., Parmigiani, A., Gonnermann, H. M., & Dufek, J. (2014). A new bubble dynamics model to study bubble growth, deformation, and coalescence. *Journal of Geophysical Research: Solid Earth*, *119*(1), 216–239. https://doi.org/10.1002/2013jb010419

Iacono-Marziano, G., Morizet, Y., Trong, E. L., & Gaillard, F. (2012a). New experimental data and semi-empirical parameterization of H_2O-CO_2 solubility in mafic melts. *Geochimica et Cosmochimica Acta*, *97*, 1–23. https://doi.org/10.1016/j.gca.2012.08.035

Iacono-Marziano, G., Morizet, Y., Trong, E. L., & Gaillard, F. (2012b). New experimental data and semi-empirical parameterization of H_2O–CO_2 solubility in mafic melts. *Geochimica et Cosmochimica Acta*, *97*, 1–23. https://doi.org/10.1016/j.gca.2012.08.035

Iacono-Marziano, G., Paonita, A., Rizzo, A., Scaillet, B., & Gaillard, F. (2010). Noble gas solubilities in silicate melts: New experimental results and a comprehensive model of the effects of liquid composition, temperature and pressure. *Chemical Geology*, *279*(3–4), 145–157. https://doi.org/10.1016/j.chemgeo.2010.10.017

Iacovino, K., Matthews, S., Wieser, P. E., Moore, G. M., & Bégué, F. (2021). VESIcal Part I: An open-source thermodynamic model engine for mixed volatile (H_2O-CO_2) solubility in silicate melts. *Earth and Space Science*, *8*(11), e2020EA001584. https://doi.org/10.1029/2020ea001584

Iacovino, K., & Till, C. B. (2019). DensityX: A program for calculating the densities of magmatic liquids up to 1,627°C and 30 kbar. *Volcanica*, *2*(1), 1–10. https://doi.org/10.30909/vol.02.01.0110

Jackson, L. E., Wadsworth, F. B., Mitchell, J., Rennie, C., Llewellin, E. W., Hess, K., & Dingwell, D. B. (2022). Bubble rise in molten glasses and silicate melts during heating and cooling cycles. *Journal of the American Ceramic Society*, *105*(12), 7238–7253. https://doi.org/10.1111/jace.18680

Jackson, M. G., Becker, T., & Steinberger, B. (2021). Spatial characteristics of recycled and primordial reservoirs in the deep mantle. *Geochemistry, Geophysics, Geosystems*, *22*(3), e2020GC009525. https://doi.org/10.1029/2020gc009525

Jambon, A., Weber, H., & Braun, O. (1986). Solubility of He, Ne, Ar, Kr and Xe in a basalt melt in the range 1250–1600°C. Geochemical implications. *Geochimica et Cosmochimica Acta*, *50*(3), 401–408. https://doi.org/10.1016/0016-7037(86)90193-6

Jones, D. W. R., & Rudge, J. F. (2020). Fast magma ascent, revised estimates from the deglaciation of Iceland. *Earth and Planetary Science Letters*, *542*, 116324. https://doi.org/10.1016/j.epsl.2020.116324

Jones, J. G. (1969). Pillow lavas as depth indicators. *American Journal of Science*, *267*(2), 181–195. https://doi.org/10.2475/ajs.267.2.181

Jones, M., Soule, S., Gonnermann, H., Roux, V. L., & Clague, D. (2018). Magma ascent and lava flow emplacement rates during the 2011 axial seamount eruption based on CO_2 degassing. *Earth and Planetary Science Letters*, *494*, 32–41. https://doi.org/10.1016/j.epsl.2018.04.044

Jones, M., Soule, S., Liao, Y., Brodsky, H., Roux, V. L., & Klein, F. (2020). Quantitative vesicle analyses and total CO_2 reconstruction in mid-ocean ridge basalts. *Journal of Volcanology and Geothermal Research*, *407*, 107109. https://doi.org/10.1016/j.jvolgeores.2020.107109

Körner, C., Thies, M., Hofmann, T., Thürey, N., & Rüde, U. (2005). Lattice Boltzmann model for free surface flow for modeling foaming. *Journal of Statistical Physics*, *121*(1–2), 179–196. https://doi.org/10.1007/s10955-005-8879-8

Kurz, M. D., Curtice, J., Fornari, D., Geist, D., & Moreira, M. (2009). Primitive neon from the center of the Galápagos hotspot. *Earth and Planetary Science Letters*, *286*(1–2), 23–34. https://doi.org/10.1016/j.epsl.2009.06.008

Lensky, N., Navon, O., & Lyakhovsky, V. (2004). Bubble growth during decompression of magma: Experimental and theoretical investigation. *Journal of Volcanology and Geothermal Research*, *129*(1–3), 7–22. https://doi.org/10.1016/s0377-0273(03)00229-4

Li, Y., Vočadlo, L., Ballentine, C., & Brodholt, J. P. (2022). Primitive noble gases sampled from ocean island basalts cannot be from the Earth's core. *Nature Communications*, *13*(1), 3770. https://doi.org/10.1038/s41467-022-31588-7

Lux, G. (1987). The behavior of noble gases in silicate liquids: Solution, diffusion, bubbles and surface effects, with applications to natural samples. *Geochimica et Cosmochimica Acta*, *51*(6), 1549–1560. https://doi.org/10.1016/0016-7037(87)90336-x

Ma, B., Liu, P., Dick, H. J. B., Zhou, M., Chen, Q., & Liu, C. (2024). Trans-lithospheric ascent processes of the deep-rooted magma plumbing system underneath the ultraslow-spreading SW Indian ridge. *Journal of Geophysical Research: Solid Earth*, *129*(1), e2023JB027224. https://doi.org/10.1029/2023jb027224

Moreira, M. A., & Kurz, M. D. (2012). The noble gases as geochemical tracers. *Advances in Isotope Geochemistry*, 371–391. https://doi.org/10.1007/978-3-642-28836-4_12

Mundl-Petermeier, A., Walker, R., Fischer, R., Lekic, V., Jackson, M., & Kurz, M. (2020). Anomalous 182W in high 3He/4He ocean island basalts: Fingerprints of Earth's core? *Geochimica et Cosmochimica Acta*, *271*, 194–211. https://doi.org/10.1016/j.gca.2019.12.020

Mutch, E. J. F., Maclennan, J., Shorttle, O., Edmonds, M., & Rudge, J. F. (2019). Rapid transcrustal magma movement under Iceland. *Nature Geoscience*, *12*(7), 569–574. https://doi.org/10.1038/s41561-019-0376-9

Neave, D. A., & Maclennan, J. (2020). Clinopyroxene dissolution records rapid magma ascent. *Frontiers in Earth Science*, *8*, 188. https://doi.org/10.3389/feart.2020.00188

Ni, H., & Keppler, H. (2013). Carbon in silicate melts. *Reviews in Mineralogy and Geochemistry*, *75*(1), 251–287. https://doi.org/10.2138/rmg.2013.75.9

Nowak, M., Schreen, D., & Spickenbom, K. (2004). Argon and CO_2 on the race track in silicate melts: A tool for the development of a CO_2 speciation and diffusion model. *Geochimica et Cosmochimica Acta*, *68*(24), 5127–5138. https://doi.org/10.1016/j.gca.2004.06.002

Nuccio, P., & Paonita, A. (2000). Investigation of the noble gas solubility in H_2O–CO_2 bearing silicate liquids at moderate pressure II: The extended ionic porosity (EIP) model. *Earth and Planetary Science Letters*, *183*(3–4), 499–512. https://doi.org/10.1016/s0012-821x(00)00297-1

Núñez-Guerrero, E., Moreira, M., & Scaillet, B. (2025). Isotopic fractionation of neon during magma degassing. *Geochemical Perspectives Letters*, *34*, 1–5. https://doi.org/10.7185/geochemlet.2505

Olson, P. L., & Sharp, Z. D. (2022). Primordial helium-3 exchange between Earth's core and mantle. *Geochemistry, Geophysics, Geosystems*, *23*(3), e2021GC009985. https://doi.org/10.1029/2021gc009985

Paonita, A. (2009). Noble gas solubility in silicate melts: A review of experimentation and theory, and implications regarding magma degassing processes. *Annals of Geophysics*, *48*(4–5), 14. https://doi.org/10.4401/ag-3225

Paonita, A., & Martelli, M. (2006). Magma dynamics at mid-ocean ridges by noble gas kinetic fractionation: Assessment of magmatic ascent rates. *Earth and Planetary Science Letters*, *241*(1–2), 138–158. https://doi.org/10.1016/j.epsl.2005.10.018

Parai, R. (2024). Noble gases in the mantle. In H. D. Holland, K. K. Turekian, R. L. Rudnick, S. B. Jacobsen, & W. F. McDonough (Eds.), *Treatise on geochemistry* (3rd ed., Vol. 1, pp. 513–564). Elsevier. https://doi.org/10.1016/b978-0-323-99762-1.00111-x

Parai, R., Mukhopadhyay, S., Tucker, J. M., & Pető, M. K. (2019). The emerging portrait of an ancient, heterogeneous and continuously evolving mantle plume source. *Lithos*, *346*, 105153. https://doi.org/10.1016/j.lithos.2019.105153

Parman, S. W. (2007). Helium isotopic evidence for episodic mantle melting and crustal growth. *Nature*, *446*(7138), 900–903. https://doi.org/10.1038/nature05691

Parmigiani, A., Faroughi, S., Huber, C., Bachmann, O., & Su, Y. (2016). Bubble accumulation and its role in the evolution of magma reservoirs in the upper crust. *Nature*, *532*(7600), 492–495. https://doi.org/10.1038/nature17401

Péron, S., Moreira, M., Colin, A., Arbaret, L., Putlitz, B., & Kurz, M. D. (2016). Neon isotopic composition of the mantle constrained by single vesicle analyses. *Earth and Planetary Science Letters*, *449*, 145–154. https://doi.org/10.1016/j.epsl.2016.05.052

Pichavant, M., Carlo, I. D., Rotolo, S. G., Scaillet, B., Burgisser, A., Gall, N. L., & Martel, C. (2013). Generation of CO_2-rich melts during basalt magma ascent and degassing. *Contributions to Mineralogy and Petrology*, *166*(2), 545–561. https://doi.org/10.1007/s00410-013-0890-5

Porcelli, D., & Halliday, A. (2001). The core as a possible source of mantle helium. *Earth and Planetary Science Letters*, *192*(1), 45–56. https://doi.org/10.1016/s0012-821x(01)00418-6

Porcelli, D., & Wasserburg, G. (1995a). Mass transfer of helium, neon, argon, and xenon through a steady-state upper mantle. *Geochimica et Cosmochimica Acta*, *59*(23), 4921–4937. https://doi.org/10.1016/0016-7037(95)00336-3

Porcelli, D., & Wasserburg, G. (1995b). Mass transfer of xenon through a steady-state upper mantle. *Geochimica et Cosmochimica Acta*, *59*(10), 1991–2007. https://doi.org/10.1016/0016-7037(95)00122-0

Qian, Y. H. (1993). Simulating thermohydrodynamics with lattice BGK models. *Journal of Scientific Computing*, *8*(3), 231–242. https://doi.org/10.1007/bf01060932

Raquin, A., & Moreira, M. (2009). Atmospheric 38ar/36ar in the mantle: Implications for the nature of the terrestrial parent bodies. *Earth and Planetary Science Letters*, *287*(3–4), 551–558. https://doi.org/10.1016/j.epsl.2009.09.003

Rybczynsk, W. (1911). On the translatory motion of a fluid sphere in a viscous medium. *Bulletin Academy Science*, *40*(33), 073605-18.

Shea, T. (2017). Bubble nucleation in magmas: A dominantly heterogeneous process? *Journal of Volcanology and Geothermal Research*, *343*, 155–170. https://doi.org/10.1016/j.jvolgeores.2017.06.025

Shea, T., Houghton, B. F., Gurioli, L., Cashman, K. V., Hammer, J. E., & Hobden, B. J. (2010). Textural studies of vesicles in volcanic rocks: An integrated methodology. *Journal of Volcanology and Geothermal Research*, *190*(3–4), 271–289. https://doi.org/10.1016/j.jvolgeores.2009.12.003

Soule, S., Nakata, D., Fornari, D., Fundis, A., Perfit, M., & Kurz, M. (2012). CO2 variability in mid-ocean ridge basalts from syn-emplacement degassing: Constraints on eruption dynamics. *Earth and Planetary Science Letters*, *327*, 39–49. https://doi.org/10.1016/j.epsl.2012.01.034

Staudacher, T., Sarda, P., Richardson, S., Allègre, C., Sagna, I., & Dmitriev, L. (1989). Noble gases in basalt glasses from a Mid-Atlantic Ridge topographic high at 14°N: Geodynamic consequences. *Earth and Planetary Science Letters*, *96*(1–2), 119–133. https://doi.org/10.1016/0012-821x(89)90127-1

Stracke, A., Willig, M., Genske, F., Béguelin, P., & Todd, E. (2022). Chemical geodynamics insights from a machine learning approach. *Geochemistry, Geophysics, Geosystems*, *23*(10), e2022GC010606. https://doi.org/10.1029/2022gc010606

Stroncik, N., & Niedermann, S. (2016). Atmospheric contamination of the primary Ne and Ar signal in mid-ocean ridge basalts and its implications for ocean crust formation. *Geochimica et Cosmochimica Acta*, *172*, 306–321. https://doi.org/10.1016/j.gca.2015.09.016

Toramaru, A. (2014). On the second nucleation of bubbles in magmas under sudden decompression. *Earth and Planetary Science Letters*, *404*, 190–199. https://doi.org/10.1016/j.epsl.2014.07.035

Tucker, J. M., & Mukhopadhyay, S. (2014). Evidence for multiple magma ocean outgassing and atmospheric loss episodes from mantle noble gases. *Earth and Planetary Science Letters*, *393*, 254–265. https://doi.org/10.1016/j.epsl.2014.02.050

Tucker, J. M., Mukhopadhyay, S., & Gonnermann, H. M. (2018). Reconstructing mantle carbon and noble gas contents from degassed mid-ocean ridge basalts. *Earth and Planetary Science Letters*, *496*, 108–119. https://doi.org/10.1016/j.epsl.2018.05.024

Voyer, M. L., Cottrell, E., Kelley, K. A., Brounce, M., & Hauri, E. H. (2015). The effect of primary versus secondary processes on the volatile content of MORB glasses: An example from the equatorial Mid-Atlantic Ridge (5°N–3°S). *Journal of Geophysical Research: Solid Earth*, *120*(1), 125–144. https://doi.org/10.1002/2014jb011160

Voyer, M. L., Hauri, E. H., Cottrell, E., Kelley, K. A., Salters, V. J. M., Langmuir, C. H., et al. (2019). Carbon fluxes and primary magma CO_2 contents along the global mid-ocean ridge system. *Geochemistry, Geophysics, Geosystems*, *20*(3), 1387–1424. https://doi.org/10.1029/2018gc007630

Wang, K., Lu, X., Liu, X., Zhou, M., & Yin, K. (2022). Partitioning of noble gases (He, Ne, Ar, Kr, Xe) during Earth's core segregation: A possible core reservoir for primordial noble gases. *Geochimica et Cosmochimica Acta*, *321*, 329–342. https://doi.org/10.1016/j.gca.2022.01.009

Wanless, V. D., & Shaw, A. M. (2012). Lower crustal crystallization and melt evolution at mid-ocean ridges. *Nature Geoscience*, *5*(9), 651–655. (Gives pressure of crystallisation below MOR. Range in Melt inclusions from 500-2500 bar. Clustering around 1500 bar.). https://doi.org/10.1038/ngeo1552

Watson, B., Sneeringer, M., & Ross, A. (1982). Diffusion of dissolved carbonate in magmas: Experimental results and applications. *Earth and Planetary Science Letters*, *61*(2), 346–358. https://doi.org/10.1016/0012-821x(82)90065-6

Watson, E. B. (2017). Diffusive fractionation of volatiles and their isotopes during bubble growth in magmas. *Contributions to Mineralogy and Petrology*, *172*(8), 61. https://doi.org/10.1007/s00410-017-1384-7

Weston, B., Burgess, R., & Ballentine, C. J. (2015). Disequilibrium degassing model determination of the 3He concentration and 3He/22Ne of the MORB and OIB mantle sources. *Earth and Planetary Science Letters*, *410*(1), 128–139. https://doi.org/10.1016/j.epsl.2014.11.021

Yamamoto, J., & Kurz, M. D. (2022). Mantle noble gas abundance ratios inferred from oceanic basalts and model estimates. *Physics of the Earth and Planetary Interiors*, *327*, 106875. https://doi.org/10.1016/j.pepi.2022.106875

Zhang, X. J., Parai, R., & Lassiter, J. C. (2024). Primordial and recycled noble gases in the cook-austral HIMU mantle: Insights into the onset of volatile subduction. *Earth and Planetary Science Letters*, *629*, 118591. https://doi.org/10.1016/j.epsl.2024.118591

Zhang, Y., & Gan, T. (2022). Diffusion in melts and magmas. *Reviews in Mineralogy and Geochemistry*, *87*(1), 283–337. https://doi.org/10.2138/rmg.2022.87.07

References From the Supporting Information

Dixon, E. T., Honda, M., McDougall, I., Campbell, I. H., & Sigurdsson, I. (2000). Preservation of near-solar neon isotopic ratios in Icelandic basalts. *Earth and Planetary Science Letters*, *180*(3-4), 309–324. https://doi.org/10.1016/s0012-821x(00)00164-3

Györe, D., Sumino, H., Yang, I., Palcsu, L., László, E., Bishop, M. C., et al. (2024). Interlaboratory re-determination of the atmospheric 22Ne/20Ne. *Chemical Geology*, *645*, 121900. https://doi.org/10.1016/j.chemgeo.2023.121900

Hiyagon, H., Ozima, M., Marty, B., Zashu, S., & Sakai, H. (1992). Noble gases in submarine glasses from midoceanic ridges and Loihi seamount: Constraints on the early history of the earth. *Geochimica et Cosmochimica Acta*, *56*(3), 1301–1316. https://doi.org/10.1016/0016-7037(92)90063-o

Honda, M., & Woodhead, J. D. (2005). A primordial solar-neon enriched component in the source of EM-i-type ocean island basalts from the Pitcairn seamounts, Polynesia. *Earth and Planetary Science Letters*, *236*(3-4), 597–612. https://doi.org/10.1016/j.epsl.2005.05.038

Jambon, A., Weber, H., & Begemann, F. (1985). Helium and argon from an Atlantic MORB glass: Concentration, distribution and isotopic composition. *Earth and Planetary Science Letters*, *73*(2-4), 255–268. https://doi.org/10.1016/0012-821x(85)90074-3

Kaneoka, I., Hanyu, T., Yamamoto, J., & Miura, Y. (2002). Noble gas systematics of the Hawaiian volcanoes based on the analysis of Loihi, Kilauea and Koolau submarine rocks. *Washington DC American Geophysical Union Geophysical Monograph Series*, *128*, 373–389. https://doi.org/10.1029/gm128p0373

Kumagai, H., & Kaneoka, I. (2003). Relationship between submarine MORB glass textures and atmospheric component of MORBs. *Chemical Geology*, *200*(1-2), 1–24. https://doi.org/10.1016/s0009-2541(03)00077-9

Kyser, T. K., & Rison, W. (1982). Systematics of rare gas isotopes in basic lavas and ultramafic xenoliths. *Journal of Geophysical Research: Solid Earth*, *87*(B7), 5611–5630. https://doi.org/10.1029/jb087ib07p05611

Macpherson, C. G., Hilton, D. R., Mertz, D. F., & Dunai, T. J. (2005). Sources, degassing, and contamination of CO_2, H_2O, He, Ne, and Ar in basaltic glasses from Kolbeinsey ridge, North Atlantic. *Geochimica et Cosmochimica Acta*, *69*(24), 5729–5746. https://doi.org/10.1016/j.gca.2005.07.015

Marty, B., & Ozima, M. (1986). Noble gas distribution in oceanic basalt glasses. *Geochimica et Cosmochimica Acta*, *50*(6), 1093–1097. https://doi.org/10.1016/0016-7037(86)90390-x

Moreira, M., & Allègre, C.-J. (2002). Rare gas systematics on mid Atlantic ridge (37–40°N). *Earth and Planetary Science Letters*, *198*(3-4), 401–416. https://doi.org/10.1016/s0012-821x(02)00519-8

Moreira, M., Staudacher, T., Sarda, P., Schilling, J.-G., & Allègre, C. J. (1995). A primitive plume neon component in MORB: The Shona ridge-anomaly, south Atlantic (51–52°S). *Earth and Planetary Science Letters*, *133*(3-4), 367–377. https://doi.org/10.1016/0012-821x(95)00080-v

Moreira, M., Valbracht, P. J., Staudacher, T., & Allègre, C. J. (1996). Rare gas systematics in red sea ridge basalts. *Geophysical Research Letters*, *23*(18), 2453–2456. https://doi.org/10.1029/96gl02301

Niedermann, S., & Bach, W. (1998). Anomalously nucleogenic neon in North Chile Ridge basalt glasses suggesting a previously degassed mantle source. *Earth and Planetary Science Letters*, *160*(3-4), 447–462. https://doi.org/10.1016/s0012-821x(98)00103-4

Niedermann, S., Bach, W., & Erzinger, J. (1997). Noble gas evidence for a lower mantle component in MORBs from the southern east pacific rise: Decoupling of helium and neon isotope systematics. *Geochimica et Cosmochimica Acta*, *61*(13), 2697–2715. https://doi.org/10.1016/s0016-7037(97)00102-6

Ozima, M., & Zashu, S. (1983). Noble gases in submarine pillow volcanic glasses. *Earth and Planetary Science Letters*, *62*(1), 24–40. https://doi.org/10.1016/0012-821x(83)90068-7

Sarda, P., Moreira, M., Staudacher, T., Schilling, J., & Allègre, C. J. (2000). Rare gas systematics on the southernmost mid-Atlantic ridge: Constraints on the lower mantle and the dupal source. *Journal of Geophysical Research: Solid Earth*, *105*(B3), 5973–5996. https://doi.org/10.1029/1999jb900282

Sarda, P., Staudacher, T., & Allègre, C. J. (1988). Neon isotopes in submarine basalts. *Earth and Planetary Science Letters*, *91*(1-2), 73–88. https://doi.org/10.1016/0012-821x(88)90152-5

Staudacher, T., Kurz, M. D., & Allègre, C. J. (1986). New noble-gas data on glass samples from Loihi seamount and Hualalai and on Dunite samples from Loihi and Rèunion Island. *Chemical Geology*, *56*(3-4), 193–205. https://doi.org/10.1016/0009-2541(86)90003-3

Stroncik, N. A., & Niedermann, S. (2016b). He, Ne and Ar isotope signatures of mid-ocean ridge basalts and their implications for upper mantle structure: A case study from the mid-Atlantic ridge at 4–12°S. *Geochimica et Cosmochimica Acta*, *183*, 94–105. https://doi.org/10.1016/j.gca.2016.04.002

Stroncik, N. A., Niedermann, S., & Haase, K. M. (2007). Neon and helium isotopes as tracers of mantle reservoirs and mantle dynamics. *Earth and Planetary Science Letters*, *258*(1-2), 334–344. https://doi.org/10.1016/j.epsl.2007.03.046

Valbracht, P., Staudigel, H., Honda, M., McDougall, I., & Davies, G. (1996). Isotopic tracing of volcanic source regions from Hawaii: Decoupling of gaseous from lithophile magma components. *Earth and Planetary Science Letters*, *144*(1-2), 185–198. https://doi.org/10.1016/0012-821x(96)00126-4

Valbracht, P. J., Staudacher, T., Malahoff, A., & Allègre, C. J. (1997). Noble gas systematics of deep rift zone glasses from Loihi seamount, Hawaii. *Earth and Planetary Science Letters*, *150*(3-4), 399–411. https://doi.org/10.1016/s0012-821x(97)00094-0